Continuum modeling of nonlinear buckling behavior of CNT using variational asymptotic method and nonlinear FEA

Renuka Sahu, Dineshkumar Harursampath & Sathiskumar A. Ponnusami

Published online: 19 May 2023.

Submit your article to this journal ⬀

Article views: 326

View related articles ⬀

View Crossmark data ⬀

Taylor & Francis
Taylor & Francis Group

ORIGINAL ARTICLE

⌀ OPEN ACCESS   Check for updates

Continuum modeling of nonlinear buckling behavior of CNT using variational asymptotic method and nonlinear FEA

Renuka Sahu[a] , Dineshkumar Harursampath[a] , and Sathiskumar A. Ponnusami[b]

[a]Department of Aerospace Engineering, Indian Institute of Science, Bengaluru, Karnataka, India; [b]Department of Engineering, City, University of London, London, UK

ABSTRACT

Carbon nanotubes (CNTs) exhibit a unique buckling behavior due to their slender tubular geometry and thin-walled circular cross section. This study aims to analyze effect of nonlinear cross-sectional deformation on buckling of CNTs. To accomplish this, CNTs are modeled as beam structures, and the analysis is conducted using the Variational Asymptotic Method (VAM) and a geometrically exact beam theory, as well as nonlinear finite element analysis (FEA). The study considers various loading cases, including pure axial compression and combined loading scenarios, such as bending-axial compression and torsion-axial compression. The results of the study indicate that inclusion of cross-sectional deformation-induced nonlinearity reduces the critical buckling load of CNTs. The reduction is 2–5% for pure axial compression and 10–40% for combined loading cases. The results are validated against existing literature and commercial finite element software, ABAQUS®. Additionally, parametric studies with different slenderness and radius-to-thickness ratios were carried out to further understand the impact of these parameters on buckling of CNTs. Finally, the study presents 3D deformed shapes of CNTs during buckling by combining the results of the 1D analysis and the 2D cross section analysis. The findings show that nonlinearity associated with radius-to-thickness ratio has a significant impact on the cross-sectional ovalisation of CNTs and is critical in evaluating their buckling behavior. This aspect of nonlinearity is often overlooked in continuum modeling methods of CNTs, making this study an important contribution to the field.

1. Introduction

CNTs, discovered by Ijima [1], are a growing class of nanomaterials characterized by their exceptionally high mechanical properties and varied geometrical nature as they can be single-walled (SWCNT), double-walled (DWCNT) or multi-walled (MWCNT). CNTs with a tubular geometry consist entirely of carbon atoms and can be functionalized with various polymeric functional groups to tailor to physical, chemical, and mechanical needs [2]. Studies show that CNTs have Young's modulus in the range of 1TPa or even higher [3, 4], with ultimate tensile strength (UTS) in the range of 100–200 GPa (theoretically). However, experimental results exhibit smaller magnitudes lying in the range of around 25–30 GPa (UTS) and 300–500 GPa for Young's Modulus, the difference being primarily due to the dependence of nanotube properties on various geometrical factors such as the chiral angle and diameter of CNT [5]. CNTs also exhibit a higher range of other mechanical properties like shear modulus [4, 6], Poisson's ratio [4, 7] and shear strength [8], which yet again depend highly on the type of CNT (SWCNT or MWCNT), its geometric parameters (radius, thickness, chirality, i.e., armchair or zigzag) and the material nonlinearities such as

defects and impurities. The waviness of CNTs also greatly impacts the mechanical performance [9], and its effect could be further intensified considering the highly nonlinear geometric range of CNTs cross section. CNTs, being multifunctional, find numerous applications, including electronics, biosensors, biomedical, and composites. Their high strength-to-weight ratio allows for ease of use in the composite and other aerospace applications, such as sensors, as structural component in composites, lightning protection systems, electromagnetic shielding and even battery applications [10–12]. Hence it becomes critical to examine their buckling behavior not only for compressive load but also combined loading cases which are more likely to occur in practice.

Various modeling approaches have been used to characterize and analyze the mechanical behavior of carbon nanotubes (CNTs), including finite element method (FEM) [13, 14] and molecular dynamics (MD) [15–19]. Giannopoulus et al. [20] developed a structural mechanics approach based on bar elements to predict elastic mechanical properties. Lee et al. [21] utilized the periodicity of the lattice structure of SWCNTs by defining repeating cell units with continuum beam elements to determine the structural properties of CNTs. A new continuum modeling method called dynamic

continuum modeling method (DCMM) was adopted and was found to determine structural properties without assuming any thickness value for the CNT. Santos et al. [22] used 1D and 3D FE models based on Euler and Timoshenko beam elements to determine the elastic moduli of SWCNTs. It was found that the Timoshenko beam element-based approach successfully determined the elastic properties, while the Euler beam element underestimated the results. Baretta et al. [23] estimated the reduced Euler–Young elastic modulus for CNTs incorporating the size dependency using the nonlocal strain gradient elasticity approach. They used a variationally consistent approach and verified the results with MD, showing that the reduced Euler-Young modulus can demonstrate both stiffness-softening and stiffness-hardening effects.

Continuum studies of CNT behavior typically use either beam models or shell models to examine the effects of various loading conditions. Bending behavior of CNTs has been studied using beam theories, such as Euler-Bernoulli, Timoshenko, and higher-order theories [24–26]. However, these studies do not account for cross-sectional deformations, even for higher-order theories. The Donnell and Sanders shell model was used to study the buckling of CNTs with a very small aspect ratio [27], and the Sanders shell theory was found to be more successful in capturing the length-dependent strains of CNTs. Li et al. [28] used traditional continuum shell theory and eigenvalue buckling methodology with elasticity parameters obtained by atomistic methods incorporated. The study shows that the continuum shell theory is efficient in predicting the post-buckling behavior of nanotubes subjected to axial compression, torsion, and bend loads, provided that the elasticity parameters of the tube are obtained from atomistic theory. Wang et al. [29] used a beam model to analyze the stability of CNTs under initial bend, and the critical axial load for kink instability, a local buckling phenomenon, was also theoretically analyzed. Wang et al. [30] used continuum elastic beam models to analyze the application of CNTs as probes in atomic force microscopes. They used a cantilever beam model to analyze SWCNT and DWCNT under a tilted compressive load to capture the phenomena of global and local buckling. The obtained results were verified with those of models considering van der Waals interaction in CNTs and were found to have good agreement, showing the applicability of the local model. Bocko et al. [31] used FEM to capture the buckling behavior of SWCNTs with beam and shell models in ANSYS® under supported boundary conditions. Wang et al. [32] used a continuum mechanics-based approach with non-convex energy theory to capture the buckling behavior of CNTs subjected to bending loads and identified the buckling modes, verifying the results with objective molecular dynamics. Yao and Han [33], taking the continuum mechanics approach, developed elastic shell models to study torsional buckling of CNTs and obtained the post-buckling equilibrium paths and buckling loads theoretically, capturing the influence of thickness on the nonlinear post-buckling behavior. Finally, Fang et al. [34] studied deformations of SWCNTs under axial and transverse forces, bending moments, and torque using FEM. Avey et al. [35] provided a theoretical investigation of the nonlinear vibration of multilayer shell-type structural elements with double curvature consisting of CNT patterned layers. They showed that the obtained frequency–amplitude relationship for multilayer spherical and hyperbolic-paraboloid shells, rectangular plate, and cylindrical panels patterned by CNTs within shear deformation and classical shell theories can be used to design and optimize the performance of nanocomposite structures.

Continuum models generally account for the interatomic forces involved in CNTs by using non-classical elasticity theories such as Eringen's nonlocal elasticity [36, 37] and Mindlin's Strain Gradient Theory [38, 39] and nonlocal strain gradient elasticity theory [40]. Micropolar elasticity theory has also been used to study the torsional [41] and bending characteristics [42] of CNTs, revealing the effect of nanotube size on its moduli. Beni et al. [43] used modified couple stress theory along with first order shear deformation shell theory to study free vibration of simply supported functionally graded nanoshell. The impactof size effect was found to be prominent in nanotubes with bigger thickness and shorter length. Eltaher et al. [44] analyzed the stability of perfect and imperfect CNTs by considering the length scale effects, micro strain and micro stress. A bottom-up nanomechanics theory called Doublet Mechanics was used and buckling loads, static response, and natural frequencies of CNTs were found out analytically. Robinson et al. [45] determined the buckling of CNTs under self-weight resting on an elastic foundation using a nonlocal Euler–Bernoulli beam model. The numerical solution was carried out using power series and differential quadrature method, demonstrating the accuracy of both methods in capturing the buckling load. Arefi et al. [46] used Eringen's nonlocal elasticity to determine the stability of initially curved CNTs under lateral load. They found that increasing the initial curvature of CNTs increases the critical buckling loads for the initial heights that cause buckling. Han et al. [47] presented a multilayer elastic shell model based on continuum mechanics to study the torsional buckling of a multiwall carbon nanotube embedded in an elastic medium. The effects of the surrounding elastic medium and van der Waals forces were taken into account. The value of the elastic constant of Winkler-type was derived, and numerical computation was carried out to estimate the critical buckling torque. Cinefra et al. [48] used a continuum approach and refined shell models obtained through Carrera's Unified Formulation to study the free vibration response of DWCNTs by modeling it as an equivalent continuum cylindrical shell. The van der Waals interaction between adjacent tubes was estimated using the Lennard-Jones model. The proposed results emphasize the differences among available continuum models and the present shell approaches used. Farajpour et al. [49] used nonlocal elasticity theory to develop a size-dependent continuum model for the nonlinear buckling of magneto-electro-elastic hybrid nanoshells in thermal environment. Effect of external electric voltage and applied magnetic potential along with the size effects on the non-dimensional buckling loads was examined. Artan et al. [50] studied curved nanotubes and determined the effect of nonlocal elasticity when the nanotube is loaded perpendicularly to its plane using the method of initial values. Azrar et al. [51] modeled the vibration characteristics of SWCMT from small to higher very higher Eigen modes by using Timoshenko and

Euler–Bernoulli beams within a nonlocal elasticity approach. These results support the idea of successfully modeling CNTs in a continuum framework but do not consider the deformation of the CNT cross-section. There has also been certain ambiguity on the application of nonlocal models to nanobeams. Romano et al. [52] analyzed the ill-posedness of the nonlocal constitutive law given by Eringen when adapted to a simple beam load case such as cantilever end-point load case. Zaera et al. [53] also analyzed this inconsistency in the nonlocal strain gradient elasticity, showing that the corresponding set of governing differential equations and boundary conditions give an over constrained problem, thus inhibiting the application of nonlocal continuum models. It is also to be noted that most of these non-classical continuum models only capture 1D deformations and not cross-sectional warping or geometrically nonlinear behaviors, which can result in reduced stiffness in CNTs.

The high slenderness ratio of CNTs results in extremely large deformation under bending loads and this nonlinear deformation seen in many shell structures [54], is intensified by cross-sectional geometrical nonlinearity due to the thin-walled nature of CNT geometry and its high radius-to-thickness ratio, causing ovalisation of the initially circular cross section [55]. This nonlinear behavior decreases stiffness and increases bending deformation even under reduced loadings, potentially leading to local buckling of the CNT and poor mechanical response of the overall structure. Harursampath et al. [56] demonstrated the impact of nonlinear cross-sectional deformations in thin beams, where the thickness-to-radius ratio $\ll 1$. They showed that nonlinear phenomena, such as the Brazier effect, first described by Brazier [57], is the nonlinear growth in the curvature of thin-walled isotropic cylindrical tubes under pure bending caused by ovalisation in the cross section, leading to collapse at a specific maximum moment. This nonlinear cross-sectional behavior becomes significant for CNTs, as they also have a small thickness-to-radius ratio, which is the main contributor to this effect. Although continuum theories successfully capture the buckling phenomena of nanoscale CNTs, they do not delve deep into the deformation shapes, geometric nonlinearity, and nonlinear effects in thin small structures, such as the Brazier effect. Atomistic models although capable of capturing exact geometry of CNTs however, are limited by the high computational time and effort requirements, which may not always be necessary to analyze continuum structures. Duan et al. [58] used a hybrid model using the classical inelastic beam and shell theory and molecular mechanics and incorporated the nature of atomic structures by fitting parameters with the MD principle. They identified the geometrical parameters for which the CNT will behave as a beam while buckling or shell upon buckling. Both these buckling modes are found to occur in CNTs and can be differentiated as: beam like buckling has that the central axis of beam deflects sideways during buckling whereas for shell like buckling the tube buckles sideways but maintains its central axis. Harik [59] established a set of geometrical conditions which define the aspect ratio and ratio of radius and thickness for CNTs to determine the applicability of the beam model based on continuum theories. It can be seen

from there criteria that the model used in current work is justified.

This article aims to present a continuum beam model utilizing VAM to capture the non-classical nonlinearity associated with the cross-sectional deformation of SWCNT and to assess its influence on buckling behavior. Previous works that modeled CNTs as continuum beams often fail to consider the cross-sectional nonlinearity though the classical nonlinearity associated with large deformation/rotations of the 1D beam is considered. In other words, the phenomena such as ovalisation and other complex deformation modes of the CNT cross sections are ignored, and *ad hoc* assumptions on how the cross sections deform are made a priori. In this work, combining the results of nonlinear cross-sectional analysis using VAM with 1D nonlinear FEA, we showcase the influence of such nonlinearities on the mechanical behavior of CNTs, particularly buckling behavior.

2. Methodology

SWCNT is assumed to be a continuum and geometry is taken to be that of a thin-walled hollow circular cross section beam. VAM is used to carry out the 2D cross-sectional analysis yielding the warping solutions, and the 1D beam analysis is done using nonlinear FEM. Critical buckling loads for pure axial compression and combined load cases of compression and bending & torsion and compression are obtained. Parametric studies have been conducted to analyze the effect of the length-to-radius (L/R) ratio and the radius-to-thickness (R/t) ratio. 3D deformed beam shapes (under axial compression and combined loading) are highlighted. Finally, comparison of the results obtained with the current work in the literature has been made to showcase the effectiveness and efficiency of the mathematical model adopted.

Overall, the modeling approach adopted here can be subdivided into VAM and FEM. Using VAM, the CNT has been characterized as a thin-walled hollow cross section beam in a continuum state. The kinematics to describe the deformation behavior of the CNT beam and geometrical non-linearity arising in the CNT behavior are accounted for using VAM. The 2D cross section analysis and expressions are derived using VAM. FEM is used for the 1D analysis of the beam. The expressions obtained from VAM analysis are then implemented in a finite element framework to derive the beam behavior for various loading conditions.

2.1. 2D cross section analysis using VAM

VAM is an extensive mathematical tool based on variational principles. It uses the inherent small parameters present in a particular problem description and hence using that tries to develop problem-specific solutions. Not that it is extremely customized to a problem, but it can also be generalized for different kinds of problems. For example, the kinematics and variational derivatives will be similar for all sorts of shell problems. Similarly, for any kind of beam, there are similar kinematic derivations. The beauty of VAM is its applicability. It offers a solution for problems ranging from

the atomic scale to cases pertaining to huge warships and aircraft. This makes VAM extremely versatile, and its accuracy and mathematical dexterity ensure highly efficient and accurate results. A summary of VAM beam analysis can be as seen in Figure 1.

Following and extending from the work of Ponnusami et al. [55], VAM analysis is carried out in broadly three parts: deriving kinematic relations for the beam, obtaining zeroth and first-order approximations for the beam warping. These are further described below.

2.1.1. Kinematic relations

Representing the CNT as a slender beam structure, Figure 2 represents the coordinate system used in this work. There are two coordinate systems, Cartesian measures represented by x_i's and polar coordinate measures represented by y_i's. The unit vectors for these coordinate systems are given by $\mathbf{a}_i$ and $\mathbf{b}_i$, respectively, (see Figure 3). The CNT is taken to have hollow circular cross-section with inner radius R_i and outer radius R_o. The thickness of the beam is given by $t = (R_o - R_i)$. The domain of the beam is given as: $0 \leq x_1 \leq L$, $-\pi R \leq y_2 \leq \pi R$ and $-(t/2) \leq y_3 \leq (t/2)$. Here, $R = (R_i + R_o)/2$ is the mean radius of the CNT.

Relation between deformed and undeformed beam configuration, is represented using the position vectors, $\hat{\mathbf{r}}$ in the undeformed configuration $\hat{\mathbf{R}}$ and in the deformed configuration (given by Eqs. 1 and 2, respectively). The same coordinate system has been defined for the deformed configuration with X_i, Y_i being the Cartesian and polar coordinate measures with unit vectors $\mathbf{A}_i$ and $\mathbf{B}_i$ respectively.

$$\hat{\mathbf{r}}(x_1, x_2, x_3) = \mathbf{r}(x_1) + x_2\mathbf{b}_2(x_1) + x_3\mathbf{b}_3(x_1)$$
$$= y_1\mathbf{a}_1 + (R + y_3)\mathbf{a}_3(y_2) \tag{1}$$

$$\hat{\mathbf{R}} = y_1\mathbf{b}_1 + u_i\mathbf{b}_i + (R + y_3)\mathbf{A}_3 + w_i(y_1, y_2, y_3)\mathbf{A}_i \tag{2}$$

Further, using the relationship $\mathbf{D} = \mathbf{G}^i\mathbf{g}_i$ and $D_{ij} = \mathbf{A}_i.\mathbf{D}.\mathbf{a}_j$, where D_{ij} is the deformation gradient tensor, $\mathbf{G}^i$ is

the covariant base vectors in the deformed configuration, $\mathbf{g}_i$ is the contravariant base vectors in the undeformed configuration, the tensor representing deformation gradient is obtained and is given as:

$$D = \begin{bmatrix} 1 + u_1' & \left(\dfrac{R}{R + y_3}\right)u_{1,2} & u_{1,3} \\ u_2' & 1 + \left(\dfrac{R}{R + y_3}\right)\left(u_{2,2} + \dfrac{u_3}{R}\right) & u_{2,3} \\ u_3' & \left(\dfrac{R}{R + y_3}\right)\left(u_{3,2} + \dfrac{u_2}{R}\right) & 1 + u_{3,3} \end{bmatrix} \tag{3}$$

The terminology used here with superscript $()'$ represent the differentiation of a quantity with x_1 or y_1 and subscript '2' or '3' refer to partial differentiation of a term with respect to y_2 and y_3, respectively. Using the deformation gradient tensor, the expression for 3D strain tensor (Γ) are obtained using the expression Eq. (4).

$$\Gamma = \frac{1}{2}\left(D^T D - I_3\right) \tag{4}$$
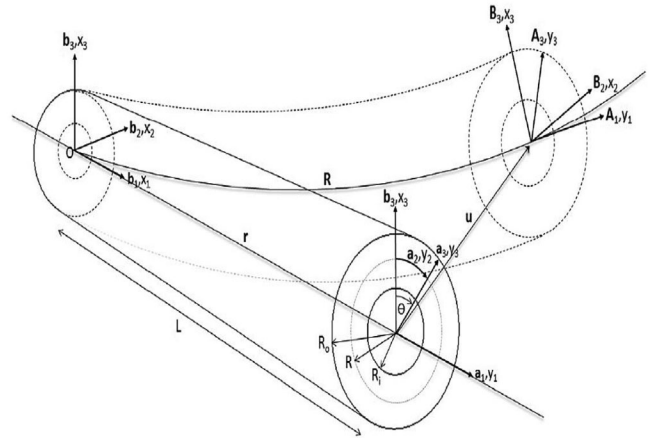
Here, I_3 is a 3 by 3 identity matrix.

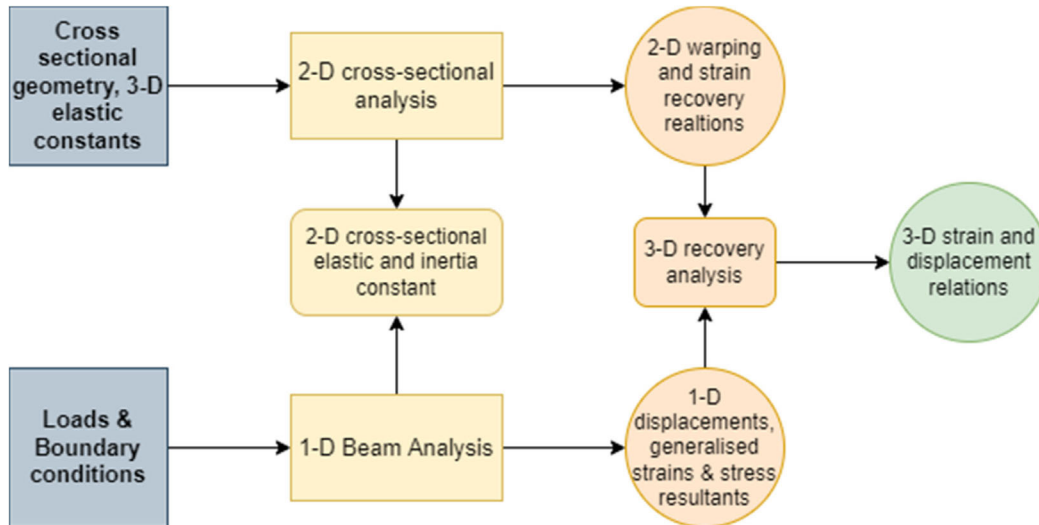Figure 2. Beam coordinate system used to model CNT.

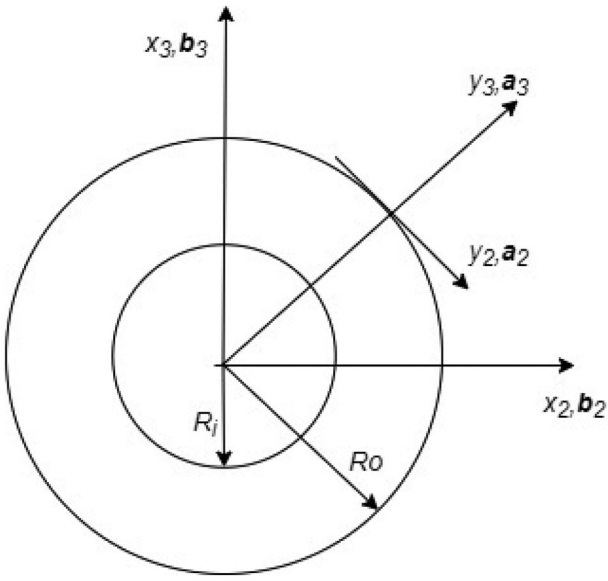Figure 1. Flowchart representing the VAM method of beam analysis.

Figure 3. Cross-sectional coordinate system of CNT.

2.1.2. Order approximation and strain energy

Order approximation can be said to be the most crucial step in the VAM analysis. With this step, the asymptotic analysis of the problem is initiated. Defining the beam strain energy as given by Eq. (5).

$$U = \frac{1}{2}\langle\langle E_{ijkl}\Gamma_{ij}\Gamma_{kl}\rangle\rangle \tag{5}$$

Here, $\langle\langle\cdot\rangle\rangle$ denotes the integration over the cross-section given by Eq. (6). E_{ijkl} is the 3D material stiffness matrix.

$$\langle\langle\cdot\rangle\rangle = \oint(.)g_0 dy_2 dy_3 \tag{6}$$

For the order analysis, the small parameters for the problem are identified. Here, there are two geometric small parameters, the radius to length ratio, $\delta_R = R/L$ and the thickness to radius ratio $\delta_t = t/R$ of the CNT. These geometric small parameters along with the order of strain are included in the strain energy expression and help to segregate the strain energy terms in the order of their magnitude. Taking strain to have a maximum order of $o(\epsilon)$ such that $\epsilon \ll 1$, the order analysis is carried out. The constraints applied on the warping variables in the VAM procedure are as follows:

$$\langle w_1 \rangle = 0 \tag{7}$$

$$\left\langle w_2\cos\frac{y_2}{R} + w_3\sin\frac{y_2}{R}\right\rangle = 0 \tag{8}$$

$$\left\langle w_3\cos\frac{y_2}{R} - w_2\sin\frac{y_2}{R}\right\rangle = 0 \tag{9}$$

$$\langle w_2(R + y_3)\rangle = 0 \tag{10}$$

Here, $\langle\cdot\rangle$ represents integration over cross-section, that is, $\int\int dy_2 dy_3$. The above constraints imply that there is no contribution of warping to the rigid body like deformation due to extension (Eq. 7), no contribution of warping to rigid body like deformation occurring as a result of bending

around x_2 direction (Eq. 8). Further warping does not contribute to rigid body like deformation due to bending about x_2 direction (Eq. 9) and due to torsion (Eq. 10).

2.1.3. Warping solutions and beam stiffness matrix

As per the above-described procedure, zeroth order approximation is carried out. Further to obtain highly accurate solution of warping/displacements first-order approximation is carried out. The displacement field obtained by first order approximation is as follows:

$$u_1^I = q_1 - q_3'\left\{(R + y_3)\sin\theta - \frac{3(R\rho)^2}{10(R\rho)^2 + 144\mu}\right.$$
$$\left.[3(R - y_3)\sin\theta - (R + 3y_3)\sin 3\theta]\right\} \tag{11}$$

$$u_2^I = q_2 + q_3\cos\theta - \frac{3(R\rho)^2}{5(R\rho)^2 + 72\mu}(R - 3y_3)\sin 2\theta \tag{12}$$

$$u_3^I = q_3\sin\theta + \frac{6(R\rho)^2}{5(R\rho)^2 + 72\mu}R\cos 2\theta \tag{13}$$

Here, $\theta = \frac{y_2}{R}$. Now, using the warping solutions from the first order approximation, the first order beam strain energy is obtained using which the 1D constitutive law for the beam can be obtained. This is given by Eq. (14).

$$U_{1D} = \frac{1}{2}\begin{Bmatrix}\gamma_{11}\\k_1\\k_2\\k_3\end{Bmatrix}^T\begin{bmatrix}2\pi R A_{11} & -2\pi R^2 A_{16} & 0 & 0\\-2\pi R^2 A_{16} & 2\pi R^3 A_{66} & 0 & 0\\0 & 0 & S_{33}(k_2) & 0\\0 & 0 & 0 & S_{33}(k_3)\end{bmatrix}\begin{Bmatrix}\gamma_{11}\\k_1\\k_2\\k_3\end{Bmatrix}$$

$$\tag{14}$$

Here, the coefficients A_{11}, A_{16}, and A_{66} are the functions of material and cross-sectional geometric parameters as defined by Harursampath [60]. Also, S_{33} is the nonlinear bending stiffness and is given by Eq. (15).

$$S_{33}(\rho) = \pi R^3 A_{11}\left[1 - \frac{9(R\rho)^2}{10(R\rho)^2 + 144\mu}\right] \tag{15}$$

The term 'ρ' is used to represent the bending curvatures k_2, k_3. Due to the axisymmetric geometry of the CNT beam, the bending stiffness in both the Cartesian coordinate directions is same, hence, the single term 'ρ' is used to represent them both. The term 'μ' is given by Eq. (16).

$$\mu = \frac{D_{22}}{R^2 A_{11}} \tag{16}$$

μ is non-dimensional in nature and is a measure of the resistance of the cross-section to deform in its own plane. Here, D_{22} is obtained from the 2D coupling stiffness matrix derived in classical laminate theory.

2.2. 1D nonlinear analysis using FEM

The global 1D nonlinear analysis of the beam is derived based on the work of Hodges [61], Cesnik and Shin [62] and Cheng [63]. For the mixed variational finite element formulation, the variational form of beam statics is represented by Eq. (17).

$$\int_0^L (\delta U_{1D} + \overline{\delta W})dx_1 = \overline{\delta A} \tag{17}$$

where W is the external work done by mechanical load per unit beam length, U_{1D} is strain energy per unit length of the beam and A is the action at the boundaries of the beam. Also, the partial derivatives of U_{1D} are defined as force and momenta resultants given by Eq. (18).

$$F_B = \left(\frac{\partial U_{1D}}{\partial \gamma}\right)^T, M_B = \left(\frac{\partial U_{1D}}{\partial k}\right)^T \tag{18}$$

Here, γ and k are the generalized strain column vectors representing linear strain and bending curvatures respectively. F_B and M_B are the internal force and moment column vectors respectively. The first element of F_B is the axial force and the second and third elements are shear forces in the deformed frame B. Similarly, the first element of M_B is the twisting moment and the second and third elements are bending moments.

Now using the following geometrical kinematic relations given by Eq. (19), one can obtain the weak form of the governing equations which facilitates the use of simplest possible shape functions.

$$\gamma = C\left(e_1 + u'_b + \tilde{k}u\right) - e_1$$

$$k = \left(\frac{\Delta - \frac{\tilde{\theta}}{2}}{1 + \frac{\theta^T\theta}{4}}\right)\theta' + Ck - k \tag{19}$$

$$C = \frac{\left(1 - \frac{\theta^T\theta}{4}\right)\Delta - \tilde{\theta} + \frac{\theta\theta^T}{2}}{1 + \frac{\theta^T\theta}{4}}$$

where C is the rotation matrix containing unknown rotation variables, θ_i and γ, k are the generalized 1D strain and curvature vectors, u_b and θ are the 1D displacement and rotation vectors. Now, the final weak form is obtained as follows:

$$\delta\Pi_b = 0$$

$$\delta\Pi_b = \int_0^L \left\{ \begin{array}{c} \delta u'_b C^T F_B + \overline{\delta\varphi_b}' C^T M_B \\ -\overline{\delta\varphi_b}' C^T(\tilde{e}_1 + \tilde{\gamma})F_B \\ -\overline{\delta F_b}^T[C^T(e_1 + \gamma) - e_1] - \overline{\delta F_b}'^T u_b - \overline{\delta M_b}^T\left(\Delta + \frac{\tilde{\theta}}{2} + \frac{\theta\theta^T}{4}\right)k \\ -\overline{\delta M_b}'\theta - \delta u_b^T f_b - \overline{\delta\varphi_b}^T m_b \end{array} \right\} dx_1 $$
$$ - \left(\delta u_b^T \widehat{F_b} + \overline{\delta\varphi_b}^T\widehat{M_b} - \overline{\delta F_b}^T\widehat{u_b} - \overline{\delta M_b}^T\hat{\theta}\right)\bigg|_0^L \tag{20}$$

Here, the generalized forces and strains are related through the constitutive relations in the following form, from which the strain measures are found and are substituted in the above equation.

$$\left\{\begin{array}{c} F_B \\ M_B \end{array}\right\} = [K]\left\{\begin{array}{c} \gamma \\ k \end{array}\right\} \tag{21}$$

The stiffness $[K]$ is in general a 6×6 matrix, depending on material distribution and cross-sectional geometry and are as derived in [62]. Now, the solutions for γ, k in terms of other measures and constants are obtained following the Eq. (22).

$$\left\{\begin{array}{c} \gamma \\ k \end{array}\right\} = [K]^{-1}\left(\left\{\begin{array}{c} F_B \\ M_B \end{array}\right\} + \left\{\begin{array}{c} F_B^{(a)} \\ M_B^{(a)} \end{array}\right\}\right) \tag{22}$$

Here, F_B and M_B are internal force and moment column vectors which are unknown variables and the actuation forces and moments $F_B^{(a)}$ and $M_B^{(a)}$ are given functions of time. For the present study, the actuation forces and moments are not accounted. These equations are substituted into Eq. (20).

Now, the beam is discretized into N number of elements and the 1D beam analysis is carried out. The discretising equation can be represented as:

$$\sum_{i=1}^N \delta\Pi_i = 0 \tag{23}$$

Here, i represents the i th element with length δl, $\delta\Pi_i$ is the spatial integration of the function over the i th element. Developing the weak formulation for spatial integration, using the shape functions given as follows, the integration was carried out. The used shape functions are:

$$x = x_i + \xi\Delta l_i, \quad dx = \Delta l_i d\xi, \quad ()' = \frac{1}{\Delta l_i}\frac{d}{d\xi}()$$

$$\delta u_b = \delta u_i(1 - \xi) + \delta u_{i+1}\xi \qquad u_b = u_i \tag{24}$$

$$\overline{\delta\varphi_b} = \overline{\delta\varphi_i}(1 - \xi) + \overline{\delta\varphi_{i+1}}\xi \qquad \theta = \theta_i$$

$$\overline{\delta F_b} = \overline{\delta F_i}(1 - \xi) + \overline{\delta F_{i+1}}\xi \qquad F_B = F_i$$

$$\overline{\delta M_b} = \overline{\delta M_i}(1 - \xi) + \overline{\delta M_{i+1}}\xi \qquad M_B = M_i$$

Here, constant shape functions are used for the displacement, rotation, force, and moment variables. Applying the above shape functions over the element and integrating will lead to following finite element form,

$$\sum_{i=1}^N \left\{ \begin{array}{c} \delta u_i^T f_{u_i} + \overline{\delta\varphi_i}^T f_{\varphi_i} + \overline{\delta F_i}^T f_{F_i} + \overline{\delta M_i}^T f_{M_i} + \delta u_{i+1}^T f_{u_{i+1}} \\ + \overline{\delta\varphi_{i+1}}^T f_{\varphi_{i+1}} + \overline{\delta F_{i+1}}^T f_{F_{i+1}} + \overline{\delta M_{i+1}}^T f_{M_{i+1}} \end{array} \right\}$$

$$= \delta u_{N+1}^T \hat{F}_{N+1} + \overline{\delta\varphi}_{N+1}^T \hat{M}_{N+1} - \overline{\delta F}_{N+1}^T \hat{u}_{N+1} - \overline{\delta M}_{N+1}^T \hat{\theta}_{N+1}$$

$$- \delta u_1^T \hat{F}_1 - \overline{\delta\varphi}_1^T \hat{M}_1 + \overline{\delta F}_1^T \hat{u}_1 + \overline{\delta M}_1^T \hat{\theta}_1 \tag{25}$$

where, f_{u_i}, f_{φ_i}..., $f_{M_{i+1}}$ are the element functions resulting from the spatial integration. The expressions for the functions are given below,

$$f_{u_i} = C^T F_i - \overline{f}, f_{u_{i+1}} = C^T F_i - \overline{f_{i+1}}$$

$$f_{\varphi_i} = -C^T M_i - \frac{\Delta l_i}{2} C^T (\tilde{e}_1 + \tilde{\gamma}) F_i - \overline{m}_i f_{\varphi_{i+1}}$$

$$= C^T M_i - \frac{\Delta l_i}{2} C^T (\tilde{e}_1 + \tilde{\gamma}) F_i - \overline{m}_{i+1}$$

$$f_{F_i} = u_i - \frac{\Delta l_i}{2} \left[C^T (e_1 + \gamma_i) - e_1 \right] f_{F_{i+1}} = -u_i - \frac{\Delta l_i}{2} \left[C^T (e_1 + \gamma_i) - e_1 \right]$$

$$f_{M_i} = \theta_i - \frac{\Delta l_i}{2} \left(\Delta + \frac{\theta_i}{2} + \frac{\theta_i \theta_i^T}{4} \right) k_i f_{M_{i+1}} = -\theta_i - \frac{\Delta l_i}{2} \left(\Delta + \frac{\theta_i}{2} + \frac{\theta_i \theta_i^T}{4} \right) k_i$$

$$(26)$$

where $\overline{f}_i, \overline{f}_{i+1}, \overline{m}_i,$ and $\overline{m}_{i+1}$ are the effective nodal load vectors resulting from external loading. A set of nonlinear algebraic equations are obtained in the following form,

$$F_S(X) - F_L = 0 \qquad (27)$$

where, F_S is the structural component, F_L is the load operator, and X is the unknown vector consisting of structural variables and is given as

$$X = \begin{bmatrix} \hat{F}_1^T & \hat{M}_1^T & u_1^T & \theta_1^T & M_1^T & \dots\dots & u_N^T & \theta_N^T & M_N^T & \hat{u}_{N+1}^T & \hat{\theta}_{N+1}^T \end{bmatrix}^T$$

$$(28)$$

Also, the explicit expression for the structural and load operator are given as,

$$F_S = \begin{Bmatrix} f_{u_1}^{(1)} + \hat{F}_1 \\ f_{\varphi_1}^{(1)} + \widehat{M}_1 \\ f_{F_1}^{(1)} - \hat{u}_1 \\ f_{M_1}^{(1)} - \hat{\theta}_1 \\ f_{u_2}^{(1)} + f_{u_2}^{(2)} \\ f_{\varphi_2}^{(1)} + f_{\varphi_2}^{(2)} \\ f_{F_2}^{(1)} + f_{F_2}^{(2)} \\ f_{M_2}^{(1)} + f_{M_2}^{(2)} \\ \cdot \\ \cdot \\ \cdot \\ f_{u_{N+1}}^{(N)} - \hat{F}_{N+1} \\ f_{\varphi_{N+1}}^{(N)} - \hat{M}_{N+1} \\ f_{F_{N+1}}^{(N)} + \hat{u}_{N+1} \\ f_{M_{N+1}}^{(N)} + \hat{\theta}_{N+1} \end{Bmatrix}, F_L = \begin{Bmatrix} \overline{f}_1^{(1)} \\ \overline{m}_1^{(1)} \\ 0 \\ 0 \\ f_2^{(1)} + f_2^{(2)} \\ m_2^{(1)} + m_2^{(2)} \\ 0 \\ 0 \\ \cdot \\ \cdot \\ \cdot \\ \cdot \\ \cdot \\ f_{N+1}^{(N)} \\ m_{N+1}^{(N)} \\ 0 \\ 0 \end{Bmatrix} \qquad (29)$$

Here, the boundary variables are represented by the hatted quantities while the others are the element variables. Also, element number is given by the superscripts and the node number is given by the subscripts.

3. Results and discussions

3.1. Validation using ABAQUS

To study the nonlinear behavior of CNTs under buckling, two different models were created in ABAQUS®: a beam model and a shell model. The beam model was designed to simulate structures with small depth and thickness compared to their length, while the shell model was intended to model thin-walled structures with exact geometric description. These models were compared to the results obtained from the current VAM-based formulation. A combined loading case was applied to the CNT, consisting of an axially compressive load and a very small bending load in the form of a uniformly distributed load along the transverse direction (x_2), to simulate the transverse displacement of the beam under combined bending and compressive loads. The variation in transverse displacement with changing axially compressive load was analyzed while keeping the bending load constant, using a mesh size of 500 elements. The CNT was modeled as an isotropic and linearly elastic material, with Young's modulus (E) = 4.88 TPa and Poisson's Ratio (v) = 0.19, and geometrical parameters of L = 200 nm, R = 1 nm, and t = 0.01 nm. The results of the analysis are shown in Figure 4, which depict the force vs. transverse displacement plots.

The comparison between the ABAQUS® shell model and the ABAQUS® beam model highlights the significant difference in the critical buckling loads. The higher critical buckling load in the beam model is attributed to its lack of consideration for the cross-sectional geometry and deformation. On the other hand, the shell model accounts for both the geometry and deformation of the cross section, providing a more accurate representation of the buckling behavior of thin-walled structures.

Figure 4 supports this difference, showing that the current work, which utilizes a VAM-based model, provides a lower critical buckling load than the ABAQUS® beam model. This is because the beam model assumes that the cross section remains perfect and does not undergo any deformation, which leads to an overestimation of its stiffness. However, the cross section of the beam does deform over time, which reduces its stiffness and results in geometrical nonlinearity. The VAM-based model takes into account this nonlinear behavior, making it a more accurate representation of the buckling behavior of CNTs. The model captures the interplay between the cross-sectional deformation and curvature, making the stiffness of the beam a function of the curvature, as expressed in Eq. (15). This enhances the accuracy of the model by considering the full extent of the nonlinear behavior, leading to a lower critical buckling load compared to the beam model.

Moreover, to ensure the validity of the nonlinear FE model developed and the convergence of the ABAQUS® simulation, mesh convergence analysis was also carried out and has been given in the appendix along with a load sensitivity study.

3.2. Validation with references

This section presents a comparison of the current work to the existing studies in the literature on the buckling of CNTs. Various methodologies have been used to study buckling in CNTs, such as MD, molecular mechanics, nonlocal theories, and FEM. The present work highlights the comparison of these works with the approach used in this article.
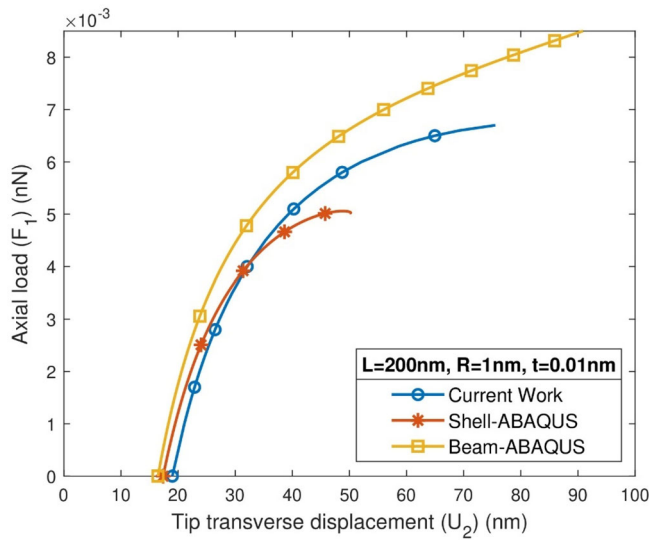
Figure 4. Axial load vs tip transverse displacement comparison with ABAQUS® shell and beam models.

Figure 5. Comparison plot with existing literature [14] showing buckling load variation with slenderness (L/R) ratio (method used in [14] is FEM).

As shown in Figure 5, the buckling load variation with different slenderness ratios of CNT is presented. The current work is validated against the study by Ansari and Rouhi [14]. They used atomistic FEM to study the axial buckling of CNT and considered a clamped-free boundary condition. The CNT parameters taken for study were a zigzag configuration with $R = 3.01412$ nm and $E = 5.488$ TPa.

In another study by Li et al. [64], the molecular structural mechanics (MSM) model was used to examine the elastic buckling behavior of CNTs. The model considered two types of CNTs: armchair and zigzag, with $t = 0.34$ nm, diameter 1 nm, and $E = 1$ TPa. Figure 6 illustrates the comparison of the buckling load variation with the slenderness ratio for the current model and the MSM models. The results show that the current model is in good agreement with the armchair configuration of CNT. However, for lower slenderness ratios (i.e., shorter CNTs), differences may occur due to the range of geometrical parameters considered in the current model's derivation. These deviations become smaller as the length of the CNT increases.

Ansari et al. [17] modeled CNTs using Eringen's nonlocal model in shell theory and determined the critical buckling load using the Rayleigh-Ritz method. It is to be noted here that the model used by Ansari is a geometrically linear one, that is, the local shell model does not consider any geometrical nonlinearity. Similarly, also for the nonlocal shell model adopted further in their work, the model is nonlocal but a geometrically linear model. The authors derived the buckling results for CNTs using MD simulations and nonlocal theory based on two nonlocal parameters, 0.35 and 0.722 [17]. The nonlocal parameters are small-scale coefficients or characteristic lengths that are used to incorporate small-size effects into the continuum framework. However, there is no consensus yet on the value of the nonlocal parameter for CNTs, so the parameters were selected after comparing the nonlocal results with MD simulations and conducting an appropriate fitting procedure to find the parameter value that produces accurate results. The parameters for single-
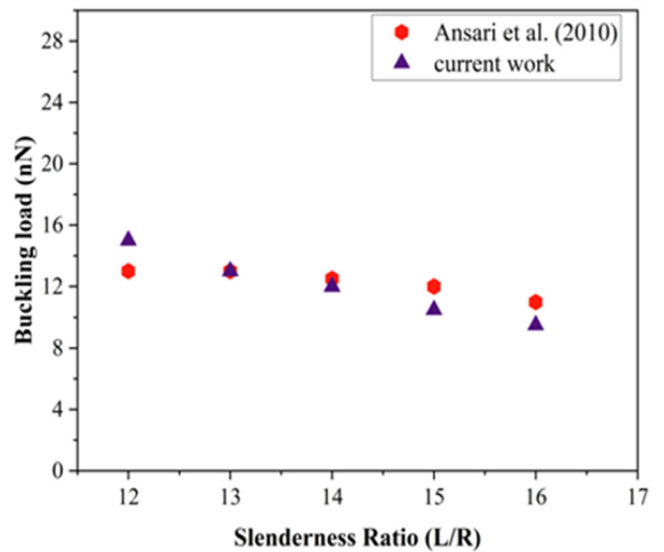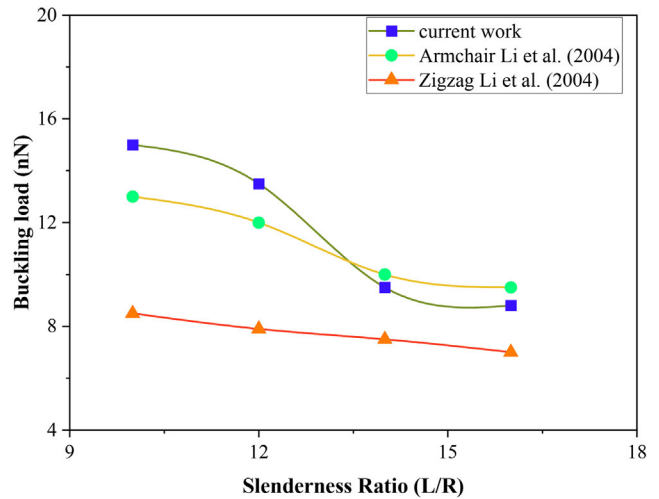

Figure 6. Comparison plot with existing literature [64] showing buckling load variation with slenderness ratio.

walled CNTs were taken as $E = 3.4$ TPa, $t = 0.1$ nm, $\nu = 0.3$, and $R = 0.5$ nm, as stated in [17]. The value of the Young's modulus was obtained using the equivalent continuum structure model of the SWCNT using 3D finite element analysis and was validated with MD results. The MD results of this work and the present nonlinear model were validated for clamped-free boundary conditions. Also, to account for a comparable model, we did geometrically nonlinear shell analysis in ABAQUS® taking same parameters in [17] for two L/R ratios. It was found that the nonlinear shell model predicted lower buckling load compared to the current work for L/R ratio 20 and this difference became significantly small as the L/R ratio increases. These results have good agreement with MD results. There is a slight discrepancy in the results of the MD model and the current model for lower values of the slenderness ratio, but this difference is negligible for higher slenderness ratio values. Additionally, there is a slight difference between the

nonlocal result reported in [17] and the current work, as the nonlocal model taken by Ansari et al. is a geometrically linear nonlocal model. It is evident that a more accurate comparison would be a geometrically nonlinear nonlocal model which is not considered in the work of [17]. Accordingly, one would expect a different value of the non-local parameter to be used in order to get an agreement with the MD results (Figure 7).

Table 1 presents the critical buckling load (P_{cr}) values obtained from the current study for different parameters taken from literature. The analysis includes both a simple compressive load and a combined loading case of twist and axial compression. The results from the current study are consistent with those obtained using FEM. However, there is a discrepancy between the results from MD simulations and nonlocal models, as the current study does not consider non-classical nonlinearities. This difference can be reduced once these effects are taken into account. From the literature study, it is evident that the current model works best for higher slenderness ratio values. This may be due to the different range of initial geometric and small parameters considered when developing the VAM based beam model.

3.3. Effect of geometrical parameters/influence of CNT geometry on buckling

This section focuses on the impact of various geometric parameters on the buckling behavior of standalone CNTs. A thorough investigation of the effect of CNT radius and thickness on the buckling load has been conducted. It was found that the buckling load is strongly influenced by these two parameters. The CNT was subjected to axial compression to simulate buckling under pure compressive loading conditions. A small perturbation load in the form of a uniformly distributed load along the transverse direction (i.e., along x_2) was applied to simulate transverse beam deflection.

The variation of buckling behavior for different R/t ratios was studied, as shown in Figure 8, keeping the length constant ($L = 200$ nm). It was observed that the buckling load decreased with an increasing R/t ratio. This result indicates that a thinner CNT is more susceptible to buckling at a smaller load compared to thicker CNTs of the same length. Figure 8 also compares the buckling loads for the cases where cross-sectional geometric nonlinearity was considered and not considered. While the results showed that accounting for cross-sectional nonlinearity gave lower buckling loads, the difference between the two cases was not substantial. For an R/t ratio of 20, the linear model predicted a higher buckling load by 2.5%, while for an R/t ratio of 80, the difference increased slightly to 5%. This highlights the presence of nonlinear geometric effects and the critical role of the small parameter R/t in the buckling behavior of CNTs.

Finally, the effect of different slenderness ratios on the critical buckling load for a CNT thickness of 0.01 nm was plotted in Figure 9. It was observed that the critical buckling load reduced with an increa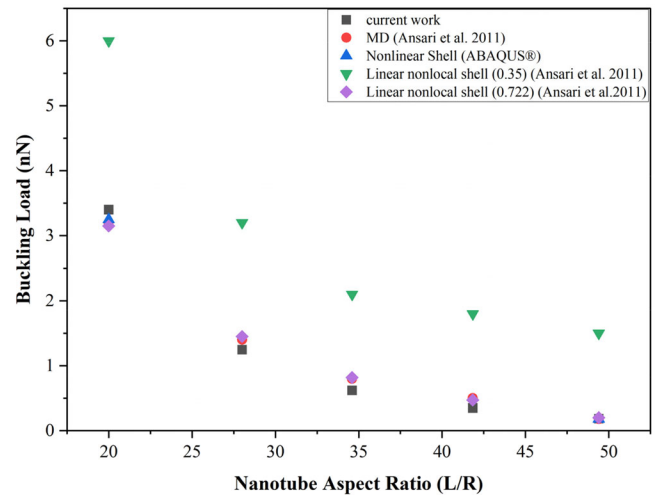se in slenderness ratio and was almost constant for higher slenderness ratios. This behavior is similar to the results reported in the works of Hu et al. [13], Ansari et al. [14], and Li et al. [64].

For an L/R ratio of 100, the buckling load decreases by 45% when cross section nonlinearity (the ovalisation of the circular cross section) is taken into account. However, for a L/R ratio of 20, that is, a shorter CNT, even after considering the nonlinear deformation of the CNT cross section, the buckling load decreases by only 2.748%. This shows that for a shorter length of CNT, the nonlinear deformation is not significant. This could be due to the dependence of the deflection of CNTs on their length. For longer CNTs, with higher transverse deflection or, in other words, higher curvature, the nonlinear stiffness term (as given by Eq. 15) increases, leading to greater deformation of the cross section and therefore quicker failure by buckling. This emphasizes the importance of incorporating geometrical nonlinearity when modeling the instability of long, slender, and thin-walled structures like CNTs.

3.4. Combined loading study with 3D representation of cross-sectional ovalisation

As seen in Section 3.3, the nonlinear geometric behavior results in changes in the buckling load. It was discovered that considering nonlinearity caused the CNT buckled at a lower axial load. However, the effect of geometric nonlinearity on simple axially compressive buckling load is significant only for higher values of R/t ratios, indicating that thinner CNTs are more susceptible to premature buckling at lower compressive loads. This is caused mainly due to deformation of the cross section leading to its ovalisation. The visualization of the cross section ovalisation phenomena is done to elaborate the extent of the 3D deformation the CNT undergoes.

The cross-sectional deformation of CNT under axial compression has been captured. Original circular cross-section is represented by the Eq. 30(a–b).

$$x_2 = R\sin\theta \tag{30a}$$

Figure 7. Comparison of current work with nonlocal and MD model.

Table 1. Critical buckling load results of current work compared with literature.

Paper	Method	Load type	L (nm)	D (nm)	P_{cr} (nN)	P_{cr} (nN) (current work)	% Diff
Yengejeh et al. [65]	FEM	Compressive	15	0.949	1.468	1.28	12.8
Yengejeh et al. [65]	FEM	Compressive	15	1.898	10.743	10.5	2.262
Mehralian et al. [66]	MD	Compressive	4.068	1.356	55	50	9.09
Mehralian et al. [66]	Nonlocal model	Compressive	5.7	1.356	29	27	6.897
Yengejeh et al. [65]	FEM	Twist + Compression	15	0.407	0.085	0.08	5.88
Yengejeh et al. [65]	FEM	Twist + Compression	15	2.171	13.8	12	13.04
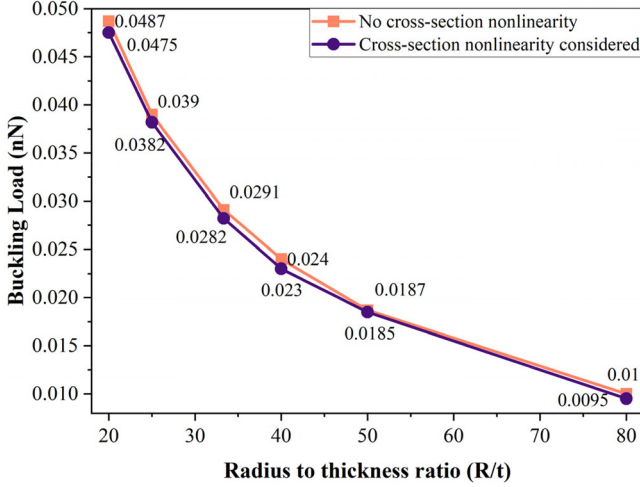
Figure 8. Variation of critical buckling load with radius to thickness (R/t) ratio.
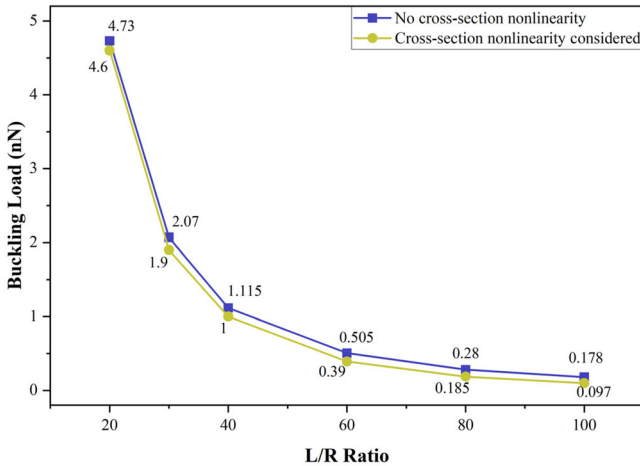
Figure 9. Variation of critical buckling load with slenderness ratio (L/R).

$$x_3 = R\cos\theta \tag{30b}$$

Using the parametric equations given by Eqs. 31(a) and 31(b), the plot for the deformed cross-section at various loads, that is, before and after buckling has been obtained,

$$X_2 = R\left(1 - \frac{\Phi_{s2}}{2}\right)\sin\theta + R\frac{\Phi_{s2}}{6}\sin 3\theta \tag{31a}$$

$$X_3 = R\left(1 + \frac{\Phi_{s2}}{2}\right)\cos\theta + R\frac{\Phi_{s2}}{6}\cos 3\theta \tag{31b}$$

where, $\Phi_{s2} = \frac{9(R\rho)^2}{5(R\rho)^2 + 72\mu}$ and the terms ρ, θ and μ are as defined in Section 2.1.3.

The deformed and undeformed cross sections have been obtained using the 1D FE code. Figure 10a, shows the load displacement curve for CNT with geometrical specifications: $L = 200$ nm, $R = 5$ nm, and $t = 0.01$ nm, when subjected to pure axial compression. Point A, B, and C (in the figure) show the various time steps, indicating the onset of buckling, and two post buckling cases respectively.

It can be clearly seen in Figure 10b that CNT's circular cross section begins to change upon onset of buckling. Moving further to post buckling loads, the cross section becomes ovalized and even takes a dumbbell shape. This depicts a highly nonlinear geometric deformation phenomenon. Attributing to the loading and CNT parameters of Figure 10, the 3D deformed shape of the same CNT beam has been obtained using the equations for each element of the beam. Combining each of such cross sections along the length the 3D deformed shape was plotted. The 3D shapes have been generated using the 3D visualization software ParaView, an open-source software for visualization of scientific data.

For the post buckling case given by Point C (in Figure 10), three different views of the fully deformed CNT under buckling load have been shown in Figure 11a–c. There can be seen small but significant transverse deformation. It is because of the high stiffness value of CNT that the transverse deformation is small. Figure 11a gives the longitudinal view (y–z plane) of the, whereas Figure 11b gives an isometric view (showing the extent of cross-sectional deformation at the fixed end) for both deformed CNT (multicolor) and undeformed CNT (grey color). Figure 11c clearly indicate the extent of cross sectional ovalisation of CNT by giving an isometric view of the deformed CNT alone. It can be clearly seen that some cross sections of CNT have deformed more and ovalisation to a large extent has occurred (Figure 11c). This effect is more predominant at cross-sections further away from the tip probably because the bending load increases as we move further from the tip. And that is the reason why the tip cross section has minimum deformation.

This section also examines the impact of combined loading conditions on the buckling behavior of the CNTs. The SWCNT will be subjected to three loading types: axial compression, torsion, and bending. The bending load is taken as a uniformly distributed load. The boundary conditions remain the same, i.e. fixed at one end and free at the other end. A twisting moment is applied at the free end to induce torsion in the beam. In addition to studying the CNT buckling in relation to different loading and geometrical parameters, the 3D deformed shapes of the CNT at the post-buckled state have also been obtained to demonstrate the extent of CNT deformation and visualize the CNT's deformation in both the longitudinal and cross-sectional directions.
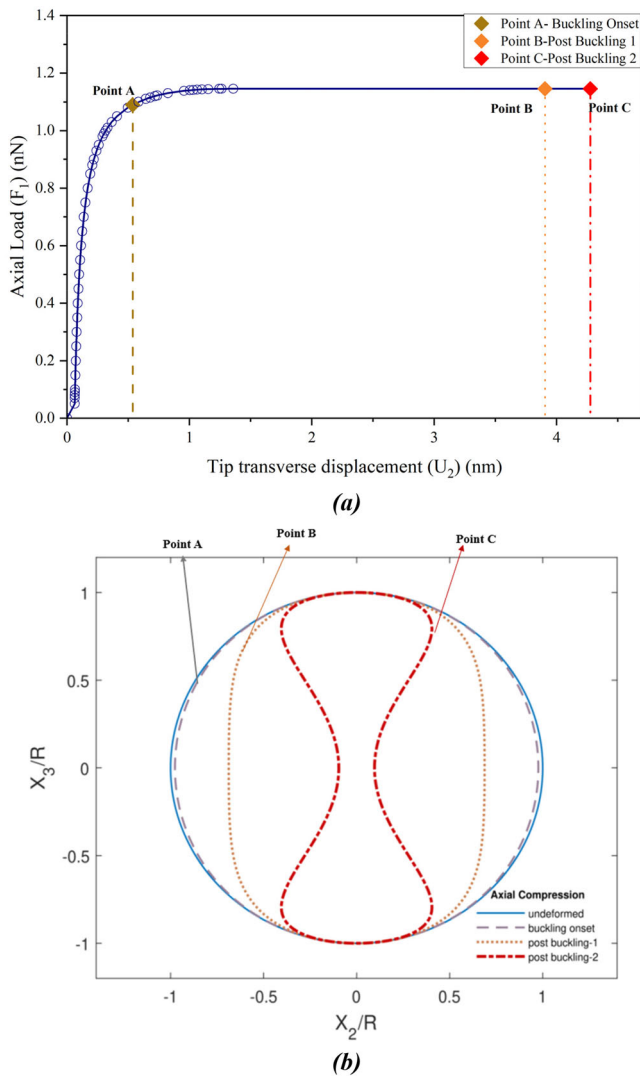
(a)

(b)

Figure 10. (a) Axial load vs tip transverse displacement curve for CNT showing different loading states. (b) CNT cross sections at different axial loads corresponding to loading states in (a).

3.4.1. Bending and axial compression

Subjecting the CNT to a uniformly distributed load along with constant axial load, a case of combined transverse loading and axial compression was created. Keeping the bending load as constant and varying the axial load, deformation of CNT was observed. Figure 12 shows the variation of CNT buckling load with different bending loads. It can be inferred from the graph that bending load plays an important role in inducing early buckling of same CNT. Upon increasing the bending load from $5*10^{-6}$ to $35*10^{-6}$ nN/nm, the buckling load decreases from 0.007 to 0.0043 nN, that is, by about 38.57%. It is evident that upon increasing the bending load, the case considering nonlinear cross section behavior diverges from the linear case where cross section nonlinearity is not considered. This indicates that the nonlinear behavior of CNT is more significant when it is subjected to bending than pure axial compression.

The extent of nonlinear behavior can be analyzed from the axial load versus the transverse displacement curves obtained for different bending loads, as shown in Figure 13, for three different bending load cases of $3*10^{-6}$ nN/nm

(a)

(b)

(c)
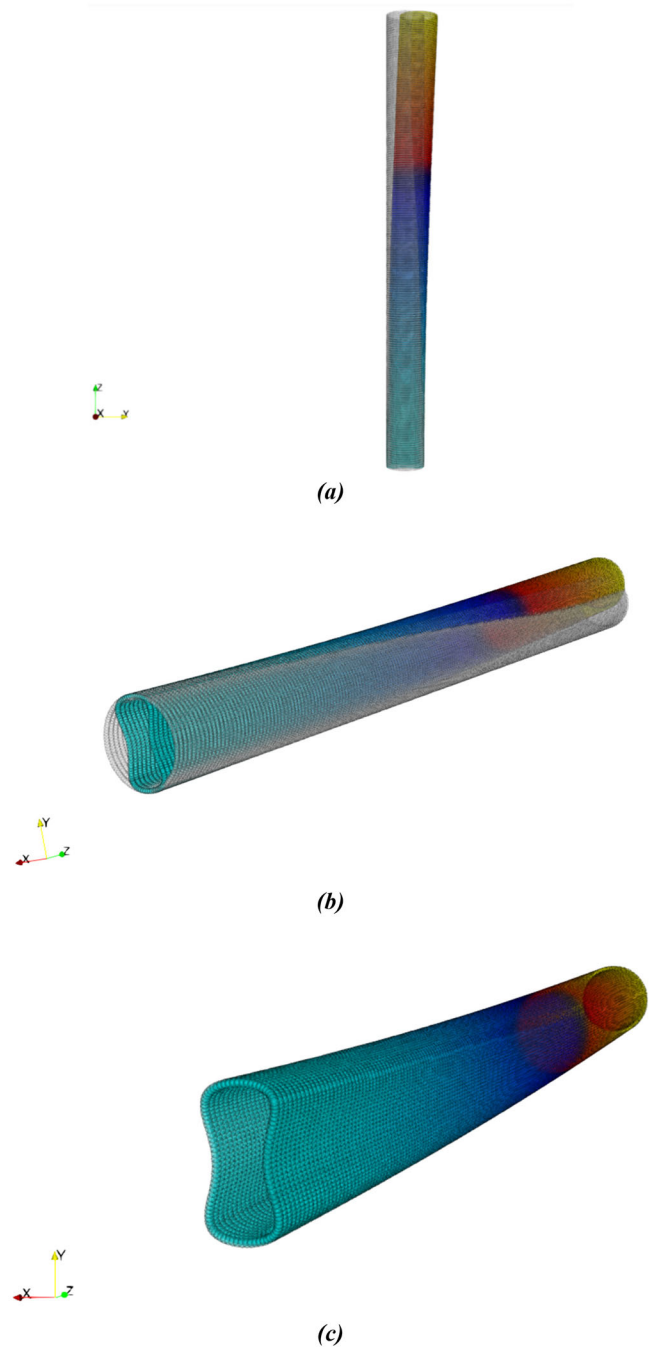
Figure 11. (a) 3D longitudinal view (*y–z* plane) of deformed CNT (multicolor) on buckling under axially compressive load (corresponding to Point C in Figure 10) compared with the undeformed CNT (grey color) (showing transverse deflection). (b) Isometric view of deformed (multicolor) and undeformed CNT (grey). (c) Isometric view of standalone deformed CNT showing ovalized cross-section.

(Figure 13a), $15*10^{-6}$ nN/nm (Figure 13b) and $25*10^{-6}$ nN/nm (Figure 13c). The effect of increasing nonlinear behavior of CNT is clearly shown by the differences in the load–displacement behaviors for the case when cross section nonlinearity is considered and when the cross section is assumed to have no deformation. This shows that for a combined load case, a higher bending load induces higher nonlinear behavior in CNT, which comes from the brazier effect. This further intensifies the buckling and eventual failure of CNT.

The influence of thickness on geometrical nonlinearity is highlighted in Figure 14, which shows the variation of buckling load with the small parameter R/t ratio. It is evident that there is a significant difference between the buckling

loads for linear and nonlinear cases. For this study, the CNT geometry with $L = 200$ nm and $R = 1$ nm was kept same and thickness was varied. It was observed that for lower R/t values, the difference in buckling loads between linear and nonlinear cases was 2.56%. However, for a higher R/t ratio of 100, this difference increased to 15.52%. The deformed cross sections for both cases were plotted along with the varying R/t ratio, demonstrating the extent of nonlinear deformation in thinner CNTs. Additionally, this combined loading scenario highlights the significant dependence of nonlinear behavior on bending loads. As the transverse load increases, nonlinear behavior becomes increasingly pronounced compared to buckling under only axial compression.

3D deformed figures for the case of R/t ratio 100 (corresponding to Figure 14) have been shown in Figure 15 for CNT subjected to combined axial compression and bending load. The bending load has been kept constant and axially compressive load was varied to identify the buckling phenomena. CNT parameters taken here are $L = 200$ nm, $t = 0.01$ nm, and $R = 1$ nm. Since here, bending is also a dominant load the extent of transverse deformation is huge compared to the previous case of pure axial loading. Three different views for the same load cases have been shown in
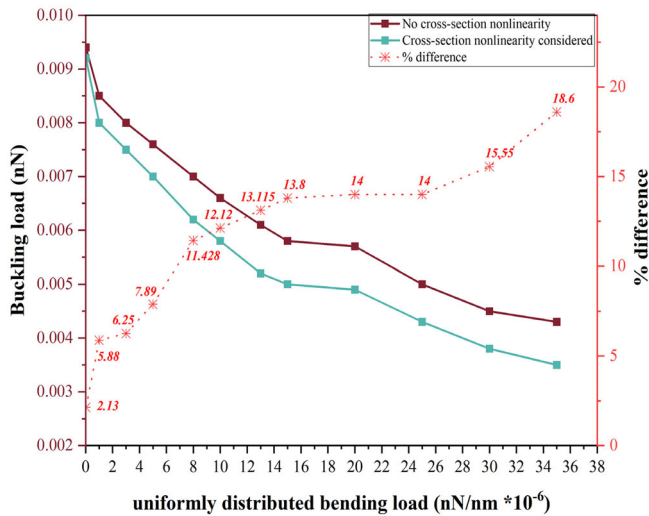
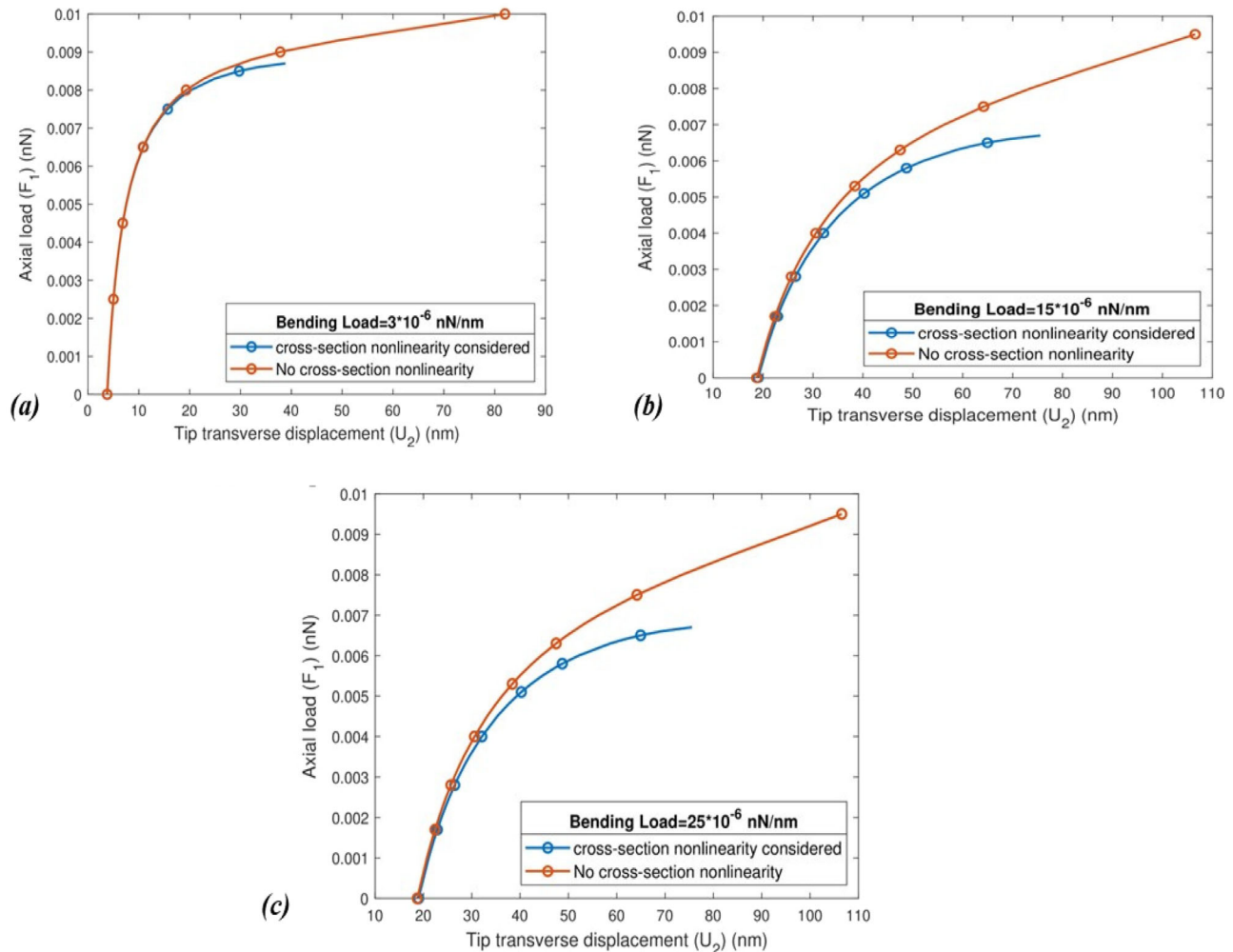**Figure 12.** Buckling load variation with bending load.

Figure 13. Axial load vs tip transverse displacement for different bending loads.

Figure 15a–c, where Figure 15a shows the extent of deformation of CNT when compared to the original undeformed shape, giving a longitudinal view (y–z plane) showing the transverse displacement. Figure 15b gives the view on the x–y plane and Figure 15c gives the isometric view of the deformed CNT. Here also the same behavior of cross-
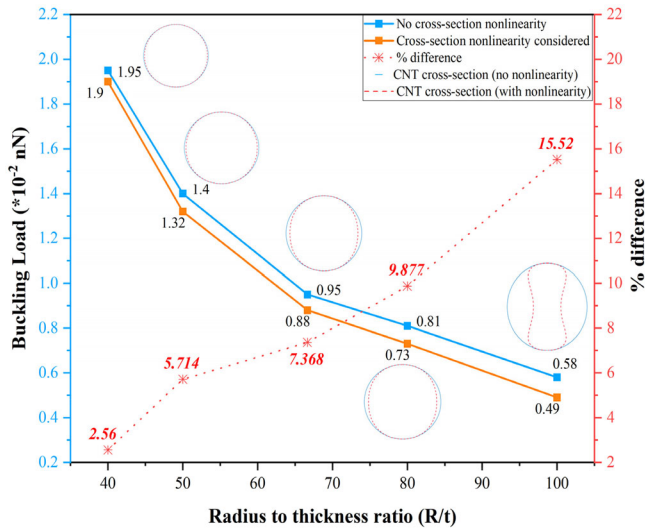

Figure 14. Variation of critical buckling load with radius to thickness (R/t) ratio for combined bending and axial compression case. Ovalisation of CNT cross section with changing thickness is also shown.
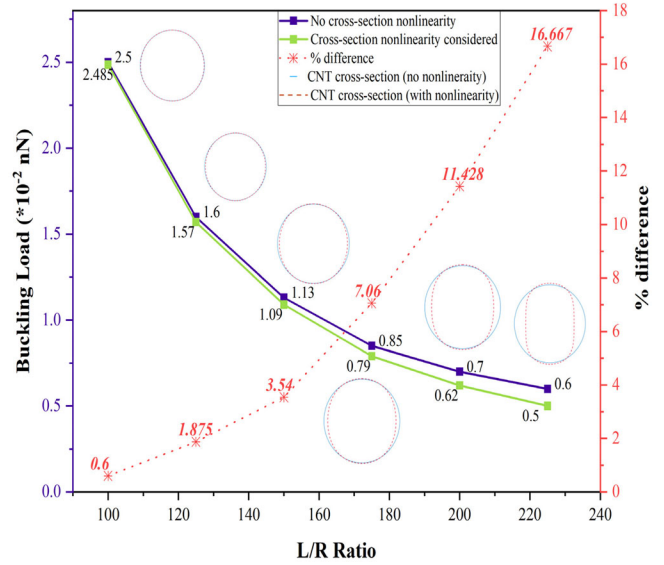
Figure 16. Variation of critical buckling load with L/R ratio for combined torsion and compression case. Ovalisation of CNT cross section with changing length is also shown.

(a)

(b)

(c)
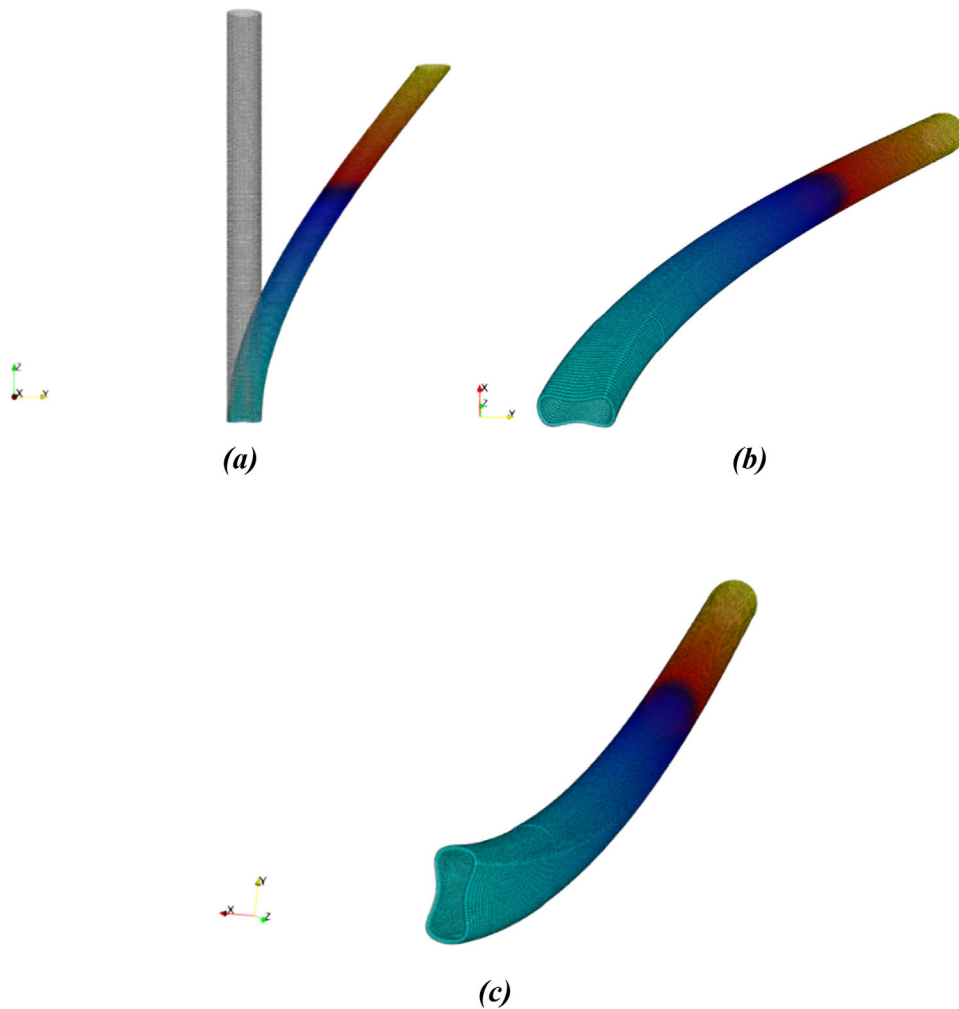
Figure 15. 3D representation of deformed CNT after buckling under combined bending and compression. (a) Longitudinal (y–z plane) view of the deformed (multi-color) and undeformed (grey) CNT. (b) x–y plane view of deformed CNT. (c) Isometric view of deformed CNT.
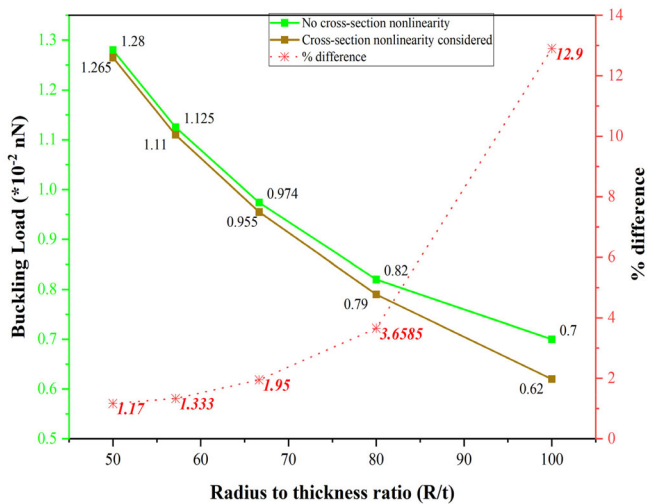
Figure 17. Variation of critical buckling load with R/t ratio for combined torsion and compression case.

sectional deformation is observed, being maximum at the fixed end and minimum at the tip of the beam.

3.4.2. Torsion and axial compression

Taking the loading case of twisting and compression, a constant torque and varying axial load is applied to simulate buckling of CNT. This is done for different slenderness ratios and the different buckling onset load for nonlinear and linear geometric behavior was obtained. The torque applied for each CNT was such as to induce an axial twist of 0.5 radians. This is as shown in Figure 16.

As evident from the graph, the difference in linear and nonlinear cases is around 0.6% for L/R ratio of 100 and increases to 16.66% for L/R ratio of 225. The cross-sectional deformation for different L/R ratios has been plotted alongside for the corresponding buckling load and shows the variation in cross section ovalisation clearly showing its
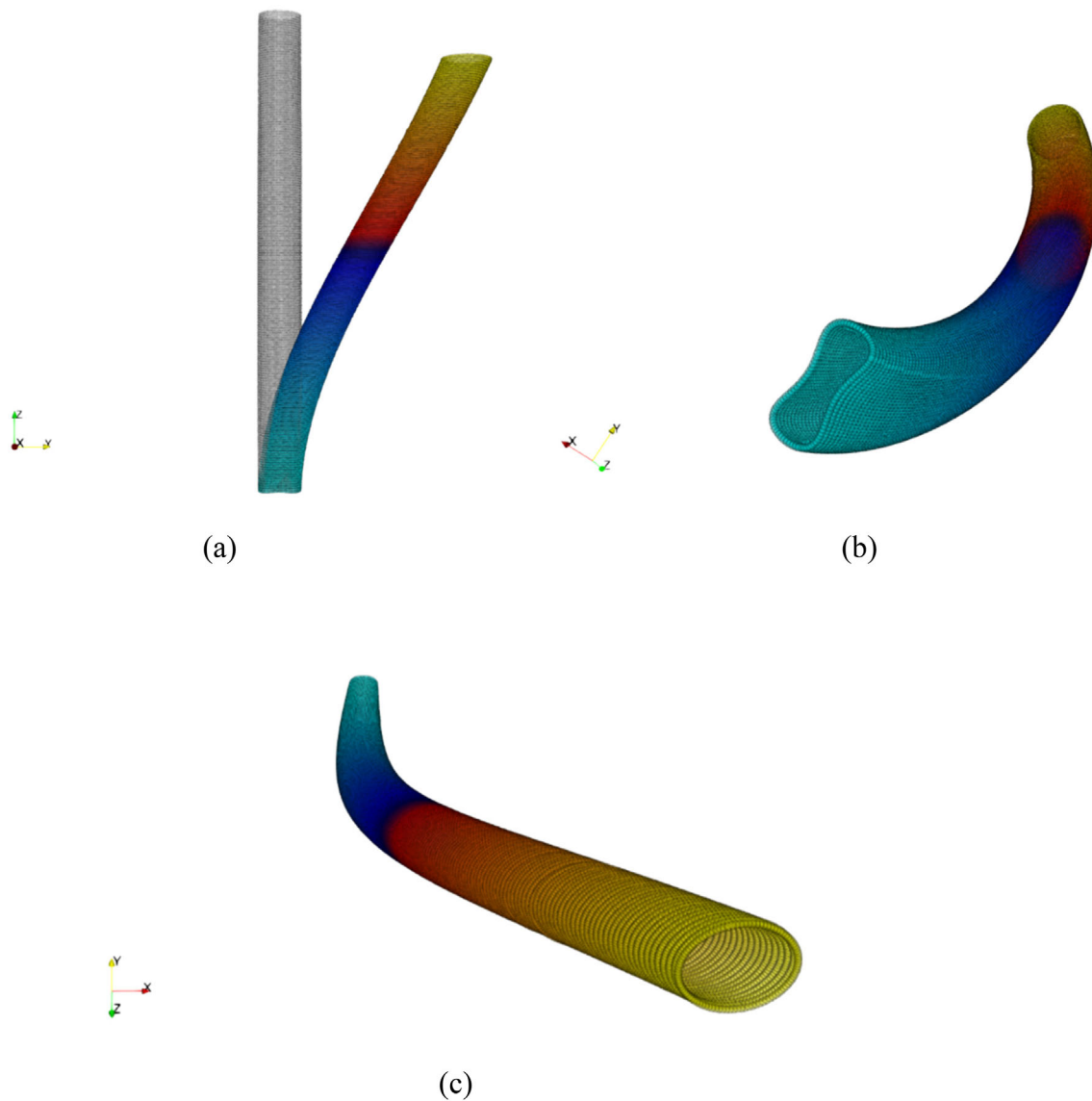
Figure 18. 3D view of deformed CNT on buckling under axial compression and torsion, (a) Longitudinal (y–z plane) view of the deformed (multicolor) and undeformed (grey) CNT, (b) Isometric view of deformed CNT, (c) x–y plane view of deformed CNT.

dependence on the length of the CNT as well. This behavior with varying CNT length is occurring for the same reasons as explained in Section 3.3. Thus, a CNT with high slenderness ratio exhibits more nonlinearity than that of CNT with lower slenderness ratio. Similarly, the process was repeated to obtain axial buckling load for different thickness value of CNTs. This is shown in Figure 17.

For the case of different R/t ratios, the variation in results for linear and nonlinear cases is more evident. This showcases the effect of thickness being superior to effect of length variation. As evident from the graph, the difference in linear and nonlinear cases is around 1.56% for R/t ratio of 50 and increases to 11.43% for R/t ratio of 100. Thus, a thinner CNT with high slenderness ratio is more prone to buckling failure. The 3D deformed CNT for the case of combined loading of torsion and axial compression for R/t ratio 100 is plotted as shown in the Figure 18. The CNT considered here has $L = 200$ nm, $R = 1$ nm, and $t = 0.01$ nm. It is found that torsion induced nonlinearity causes deformation along the x_2 direction as well, which is expected due to the twisting nature of the loading. This may lead to bulging of CNT at some location and twisting and dumbbell type structural shape at other locations. It has been observed that the dumbbell shape is found closer to the fixed end whereas bulge is found closer to the free end. Figure 18a gives the longitudinal view (y–z plane) of deformed (multi-color) and undeformed (grey) CNT. The isometric view of the standalone deformed CNT at post buckling state (for the same load case), showing transverse deflection and the deformed cross section is shown in Figure 18b. Figure 18c shows the deformed CNT from the free end where cross section deformation is minimum.

The combined loading study indicates a predominant role of bending in inducing geometrically nonlinear behavior especially at higher slenderness ratios and lower thickness values of CNT. Moreover, upon decreasing CNT thickness and radius and increasing the length, the nonlinear mechanical behavior of CNT escalates.

4. Future scope

Current research focuses on the nonlinear geometric instability in SWCNTs. This research uses a complete continuum approach, which can be applied to MWCNTs to study deformation and interactions between layers. In order to further study the impact of geometrical nonlinearity on the mechanical behavior of CNT composites, the VAM-based method can be extended. The proposed methodology can also be used to investigate the premature failure of CNT composites caused by fiber-matrix debonding. The existing modeling approach can be improved by incorporating nonlocal theories, which would allow for the integration of geometrical nonlinearity with material nonlinearity and account for small-size effects in solids due to nonbonded interactions. A comprehensive mathematical study is underway to capture the nonlinearities associated with CNTs more effectively by incorporating nonlocal theories within a continuum framework.

However, it must also be pointed out that though the nonlocal/size effects are significant in problems involving CNTs, their incorporation may not always be mandatory for all kinds of loading & support boundary conditions. In fact, nonlocal/size effects may become an overkill for certain important problems, such as the one that our work focuses on. Unnecessarily incorporating such effects renders the solution process computationally inefficient. Analogous to how the already well-established nonlinear domain decomposition method identifies & demarcates abstract problem subdomains wherein the computationally intensive nonlinear model is essential (and thus complementarily where it isn't), one can propose the new concept of a *nonlocal domain decomposition methodology*, which is one of the objectives of our further research.

5. Conclusions

The nonlinear buckling behavior of CNTs has been thoroughly analyzed in this work using VAM and nonlinear FEA. The findings highlight the crucial role of cross-sectional ovalisation in the premature failure of CNTs. It was observed that the critical buckling load decreases with increasing slenderness ratios, emphasizing the need to consider nonlinearities in CNT buckling analysis. Furthermore, the results demonstrate the significance of the R/t ratio, which governs the non-classical geometric nonlinearity, in capturing the nonlinear buckling behavior of SWCNTs. Some of the key observations are summarized as follows:

- The consideration of cross-sectional nonlinearity is vital for CNTs as it affects the critical buckling load. The difference between linear and nonlinear cases ranges from 2 to 5% for pure axial compression but can be as high as 10–40% for combined loading cases.
- The study of CNTs under different loads revealed that bending loads have the most pronounced impact on cross-sectional nonlinear geometric behavior.
- The proposed approach effectively captures the nonlinear geometric nonlinearities associated with the slenderness ratio (L/R) and the R/t ratio.
- The results of the current work have been validated against existing works in literature, such as FEM, MD, MSM, and nonlocal models, demonstrating the accuracy and reliability of the VAM and FEA in analyzing CNT buckling.

In conclusion, the proposed nonlinear modeling method using VAM and FEA provides a more engineer-friendly way to analyze the nonlinear buckling behavior of CNTs and other nanostructures. While non-local effects are important to analyze CNTs or structures of similar length scale, the present results agree well with MD simulations, implying that non-local effects may not become a significant factor for certain load cases. This aspect deserves further research and our ongoing work on non-local asymptotic modeling aims to elucidate the importance of the non-local

parameters in the context of asymptotic-correctness of the reduced-order non-local structural models.

As CNTs are increasingly explored for their potential applications in advanced composites and multifunctional structures, it becomes imperative to consider such nonlinearities in the design process. The findings of this study contribute to the advancement of knowledge in this field and provide valuable insights for future research in the area.

ORCID

Renuka Sahu http://orcid.org/0000-0002-1090-9475
Dineshkumar Harursampath http://orcid.org/0000-0001-6855-303X
Sathiskumar A. Ponnusami http://orcid.org/0000-0002-2143-8971

References

[1] S. Iijima, Helical microtubules of graphitic carbon, Nature, vol. 354, no. 6348, pp. 56–58, 1991. DOI: 10.1038/354056a0.

[2] A. Kumar, K. Sharma, and A.R. Dixit, A review on the mechanical properties of polymer composites reinforced by carbon nanotubes and graphene, Carbon Lett., vol. 31, no. 2, pp. 149–165, 2021. DOI: 10.1007/s42823-020-00161-x.

[3] E.T. Thostenson, Z. Ren, and T.-W. Chou, Advances in the science and technology of carbon nanotubes and their composites: a review, Compos. Sci. Technol., vol. 61, no. 13, pp. 1899–1912, 2001. DOI: 10.1016/S0266-3538(01)00094-X.

[4] Y. Wu, X. Zhang, A.Y.T. Leung, and W. Zhong, An energy-equivalent model on studying the mechanical properties of single-walled carbon nanotubes, Thin-Walled Struct., vol. 44, no. 6, pp. 667–676, 2006. DOI: 10.1016/j.tws.2006.05.003.

[5] A. Takakura, K. Beppu, T. Nishihara, A. Fukui, T. Kozeki, T. Namazu, Y. Miyauchi, and K. Itami, Strength of carbon nanotubes depends on their chemical structures, Nat. Commun., vol. 10, pp. 3040, 2019. https://www.nature.com/articles/s41467-019-10959-7

[6] A. Ghavamian, M. Rahmandoust, and A. Ochsner, On the determination of shear modulus of carbon nanotubes, Compos. Part B Eng., vol. 44, no. 1, pp. 52–59, 2013. DOI: 10.1016/j.compositesb.2012.07.040.

[7] X. Lei, T. Natsuki, J. Shi, and Q. Ni, Analysis of carbon nanotubes on the mechanical properties at atomic scale, Nanotechnol. Tissue Eng. Appl., vol. 2011, pp. 1–10, 2011. DOI: 10.1155/2011/805313.

[8] M. Zu, Q. Li, Y. Zhu, M. Dey, G. Wang, W. Lu, J.M. Deitzel, J.W. Gillespie Jr., J.-H. Byun, and T.-W. Chou, The effective interfacial shear strength of carbon nanotube fibres in an epoxy matrix characterised by a microdroplet test, Carbon, vol. 50, no. 3, pp. 1271–1279, 2012. DOI: 10.1016/j.carbon.2011.10.047.

[9] M. Brcic, M. Canadija, and J. Brnic, Influence of waviness and vacancy defects on carbon nanotubes properties, Procedia Eng., vol. 100, pp. 213–219, 2015. DOI: 10.1016/j.proeng.2015.01.360.

[10] M. Bottini, A. Magrini, A.D. Venere, S. Bellucci, M.I. Dawson, N. Rosato, A. Bergamaschi, and T. Mustelin, Synthesis and characterization of supramolecular nanostructures of carbon nanotubes and ruthenium-complex luminophores, J. Nanosci. Nanotechnol., vol. 6, no. 5, pp. 1381–1386, 2006. DOI: 10.1166/jnn.2006.164.

[11] K.-T. Lau, and D. Hui, The revolutionary creation of new advanced materials – carbon nanotube composites, Composites Part B, vol. 33, no. 4, pp. 263–277, 2002. DOI: 10.1016/S1359-8368(02)00012-4.

[12] M.J. Biercuk, M.C. Llaguno, M. Radosavljevic, J.K. Hyun, A.T. Johnson, and J.E. Fischer, Carbon nanotube composites for thermal management, Appl. Phys. Lett., vol. 80, no. 15, pp. 2767–2769, 2002. DOI: 10.1063/1.1469696.

[13] N. Hu, K. Nunoya, D. Pan, T. Okabe, and H. Fukunaga, Prediction of buckling characteristics of carbon nanotubes, Int. J. Solids Struct., vol. 44, no. 20, pp. 6535–6550, 2007. DOI: 10.1016/j.ijsolstr.2007.02.043.

[14] R. Ansari, and S. Rouhi, Atomistic finite element model for axial bucking of single-walled carbon nanotubes, Physica E, vol. 43, no. 1, pp. 58–69, 2010. DOI: 10.1016/j.physe.2010.06.023.

[15] Y. Wang, X. Wang, X. Ni, and H. Wu, Simulation of the elastic response and the buckling modes of single-walled carbon nanotubes, Comput. Mater. Sci., vol. 32, no. 2, pp. 141–146, 2005. DOI: 10.1016/j.commatsci.2004.08.005.

[16] H. Xin, Q. Han, and X. Yao, Buckling and axially compressive properties of perfect and defective single-walled carbon nanotubes, Carbon, vol. 45, no. 13, pp. 2486–2495, 2007. DOI: 10.1016/j.carbon.2007.08.037.

[17] R. Ansari, S. Sahmani, and H. Rouhi, Rayleigh-Ritz axial buckling analysis of single-walled carbon nanotubes with different boundary conditions, Phys. Lett. A, vol. 375, no. 9, pp. 1255–1263, 2011. DOI: 10.1016/j.physleta.2011.01.046.

[18] M. Eftekhari, S. Mohammadi, and R.A. Khoei, Effect of defects on the local shell buckling and post-buckling behaviour of single and multi-walled carbon nanotubes, Comput. Mater. Sci., vol. 79, pp. 736–744, 2013. DOI: 10.1016/j.commatsci.2013.07.034.

[19] F. Mehralian, Y.T. Beni, and Y. Kiani, Thermal buckling behavior of defective CNTs under pre-load: a molecular dynamics study, J. Mol. Graph Model., vol. 73, pp. 30–35, 2017. DOI: 10.1016/j.jmgm.2017.01.017.

[20] G.I. Giannopoulos, A.P. Tsiros, and S.K. Georgantzinos, Prediction of elastic mechanical behavior and stability of single-walled carbon nanotubes using bar elements, Mech. Adv. Mater. Struct., vol. 20, no. 9, pp. 730–741, 2013. DOI: 10.1080/15376494.2012.676714.

[21] U. Lee, and H. Oh, Evaluation of the structural properties of single-walled carbon nanotubes using a dynamic continuum modeling method, Mech. Adv. Mater. Struct., vol. 15, no. 2, pp. 79–87, 2008. DOI: 10.1080/15376490701706654.

[22] J. V. A. dos Santos, Effective elastic moduli evaluation of single walled carbon nanotubes using flexural vibrations, Mech. Adv. Mater. Struct., vol. 18, no. 4, pp. 262–271, 2011. DOI: 10.1080/15376494.2010.483326.

[23] R. Barretta, S. Ali Faghidian, F. Marotti de Sciarra, and F.P. Pinnola, Timoshenko nonlocal strain gradient nanobeams: variational consistency, exact solutions and carbon nanotube Young moduli, Mech. Adv. Mater. Struct., vol. 28, no. 15, pp. 1523–1536, 2021. DOI: 10.1080/15376494.2019.1683660.

[24] M. Mohammadimehr, A.A. Mohammadi-Dehabadi, S.M. Akhavan Alavi, K. Alambeigi, M. Bamdad, R. Yazdani and S. Hanifehlou, Bending, buckling, and free vibration analyses of carbon nanotube reinforced composite beams and experimental tensile test to obtain the mechanical properties of nanocomposite, Steel Compos. Struct., vol. 29, no. 3, pp. 405–422, 2018.

[25] N. Mohamed, S.A. Mohamed, and M.A. Eltaher, Buckling and post-buckling behaviours of higher order carbon nanotubes using energy-equivalent model, Eng. Comput., vol. 37, no. 4, pp. 2823–2836, 2021. DOI: 10.1007/s00366-020-00976-2.

[26] X. Yao, Q. Han, and H. Xin, Bending buckling behaviours of single- and multi-walled carbon nanotubes, Comput. Mater. Sci., vol. 43, no. 4, pp. 579–590, 2008. DOI: 10.1016/j.commatsci.2007.12.019.

[27] N. Silvestre, C.M. Wang, Y.Y. Zhang, and Y. Xiang, Sanders shell model for buckling of single-walled carbon nanotubes with small aspect ratio, Compos. Struct., vol. 93, no. 7, pp. 1683–1691, 2011. DOI: 10.1016/j.compstruct.2011.01.004.

[28] C. Li, and W. Guo, Continuum Mechanics Simulation of Post-buckling of Single-Walled Nanotubes, Int. J. Nonlinear Sci. Numer. Simul., vol. 4, pp. 387–393, 2003.

[29] Q. Wang, F. Xu, and G.Y. Zhou, Continuum model for stability analysis of carbon nanotubes under initial bend, Int. J. Struct. Stabil. Dyn., vol. 05, no. 04, pp. 579–595, 2005. DOI: 10.1142/S0219455405001738.

[30] Q. Wang, and V.K. Varadan, Stability analysis of carbon nanotube probes for an atomic force microscope via a continuum model, Smart Mater. Struct., vol. 14, no. 6, pp. 1196–1203, 2005. DOI: 10.1088/0964-1726/14/6/012.

[31] J. Bocko, and P. Lengvarsky, Buckling of single-walled carbon nanotubes with and without defects, J. Mech. Sci. Technol., vol. 31, no. 4, pp. 1825–1833, 2017. DOI: 10.1007/s12206-017-0330-y.

[32] C.G. Wang, Y.P. Liu, J. Al-Ghalith, T. Dumitrică, M.K. Wadee, and H.F. Tan, Buckling behaviour of carbon nanotubes under bending: from ripple to kink, Carbon, vol. 102, pp. 224–235, 2016. DOI: 10.1016/j.carbon.2016.02.041.

[33] X. Yao, and Q. Han, A continuum mechanics nonlinear postbuckling analysisfor single-walled carbon nanotubes under torque, Eur. J. Mech. A Solids, vol. 27, no. 5, pp. 796–807, 2008. DOI: 10.1016/j.euromechsol.2007.11.012.

[34] C. Fang, A. Kumar, and S. Mukherjee, A finite element analysis of single-walled carbon nanotube deformation, J. Appl. Mech., vol. 78, no. 3, pp. 1609–1614, 2011.

[35] M. Avey, N. Fantuzzi, A.H. Sofiyev, and N. Kuruoglu, Nonlinear vibration of multilayer shell-type structural elements with double curvature consisting of CNT patterned layers within different theories, Compos. Struct., vol. 275, pp. 114401, 2021. DOI: 10.1016/j.compstruct.2021.114401.

[36] M. Eltaher, S. El-Borgi, and J. Reddy, Nonlinear analysis of size-dependent and material-dependent nonlocal CNTs, Compos. Struct., vol. 153, pp. 902–913, 2016. DOI: 10.1016/j.compstruct.2016.07.013.

[37] R. Li, and G.A. Kardomateas, Thermal buckling of multi-walled carbon nanotubes by nonlocal elasticity, J. Appl. Mech., vol. 74, no. 3, pp. 399–405, 2007. DOI: 10.1115/1.2200656.

[38] B. Akgöz, and Ö. Civalek, Bending analysis of embedded carbon nanotubes resting on anelastic foundation using strain gradient theory, Acta Astronaut., vol. 119, pp. 1–12, 2016. DOI: 10.1016/j.actaastro.2015.10.021.

[39] H.M. Ouakad, S. El-Borgi, S.M. Mousavi, and M.I. Friswell, Static and dynamic response of CNT nanobeam using nonlocal strain and velocity gradient theory, Appl. Math. Model., vol. 62, pp. 207–222, 2018. DOI: 10.1016/j.apm.2018.05.034.

[40] F. Mehralian, Y.T. Beni, and M.K. Zeverdejani, Nonlocal strain gradient theory calibration using molecular dynamics simulation based on small scale vibration of nanotubes, Physica B, vol. 514, pp. 61–69, 2017. DOI: 10.1016/j.physb.2017.03.030.

[41] R. Izadi, M. Tuna, P. Trovalusci, and E. Ghavanloo, Torsional characteristics of carbon nanotubes: micropolar elasticity models and molecular dynamics simulation, Nanomaterials, vol. 11, no. 2, pp. 453, 2021. DOI: 10.3390/nano11020453.

[42] R. Izadi, M. Tuna, P. Trovalusci, and N. Fantuzzi, Bending characteristics of carbon nanotubes: micropolar elasticity models and molecular dynamics simulations, Mech. Adv. Mater. Struct., vol. 30, no. 1, pp. 189–206, 2023. DOI: 10.1080/15376494.2021.2011499.

[43] Y.T. Beni, F. Mehralian, and H. Razavi, Free vibration analysis of size-dependent shear deformable functionally graded cylindrical shell on the basis of modified couple stress theory, Compos. Struct., vol. 120, pp. 65–78, 2015. DOI: 10.1016/j.compstruct.2014.09.065.

[44] M.A. Eltaher, and N. Mohamed, Nonlinear stability and vibration of imperfect CNTs by Doublet mechanics, Appl. Math. Comput., vol. 382, pp. 125311, 2020. DOI: 10.1016/j.amc.2020.125311.

[45] M.T.A. Robinson, T.P. Kisito, K.Y. Laurent, and S. Adali, Analysis of the buckling of carbon nanotube under self-weight: the power series and differential quadrature approaches, Mech Adv Mater Struct., vol. 26, no. 10, pp. 834–841, 2019. DOI: 10.1080/15376494.2018.1430263.

[46] A. Arefi, and H. Nahvi, Stability analysis of an embedded single-walled carbon nanotube with small initial curvature based on nonlocal theory, Mech. Adv. Mater. Struct., vol. 24, no. 11, pp. 962–970, 2017. DOI: 10.1080/15376494.2016.1196800.

[47] Q. Han, X. Yao, and L. Li, Theoretical and numerical study of torsional buckling of multiwall carbon nanotubes, Mech. Adv. Mater. Struct., vol. 13, no. 4, pp. 329–337, 2006. DOI: 10.1080/15376490600675257.

[48] M. Cinefra, E. Carrera, and S. Brischetto, Refined shell models for the vibration analysis of multiwalled carbon nanotubes, Mech. Adv. Mater. Struct., vol. 18, no. 7, pp. 476–483, 2011. DOI: 10.1080/15376494.2011.604601.

[49] A. Farajpour, A. Rastgoo, and M.R. Farajpour, Nonlinear buckling analysis of magneto-electro-elastic CNT-MT hybrid nanoshells based on the nonlocal continuum mechanics, Compos. Struct., vol. 180, pp. 179–191, 2017. DOI: 10.1016/j.compstruct.2017.07.100.

[50] R. Artan, and A. Tepe, Nonlocal effects in curved single-walled carbon nanotubes, Mech. Adv. Mater. Struct., vol. 18, no. 5, pp. 347–351, 2011. DOI: 10.1080/15376494.2010.516885.

[51] A. Azrar, L. Azrar, and A. Aljinaidi, Analytical and numerical modeling of higher order free vibration characteristics of single-walled carbon nanotubes, Mech. Adv. Mater. Struct., vol. 23, no. 11, pp. 1245–1262, 2016. DOI: 10.1080/15376494.2015.1068405.

[52] G. Romano, R. Barretta, M. Diaco, and F. Marotti de Sciarra, Constitutive boundary conditions and paradoxes in nonlocal elastic nanobeams, Int. J. Mech. Sci., vol. 121, pp. 151–156, 2017. DOI: 10.1016/j.ijmecsci.2016.10.036.

[53] R. Zaera, Ó. Serrano, and J. Fernández-Sáez, On the consistency of the nonlocal strain gradient elasticity, Int. J. Eng. Sci., vol. 138, pp. 65–81, 2019. DOI: 10.1016/j.ijengsci.2019.02.004.

[54] A. Vaziri, Mechanics of highly deformed elastic shells, Thin-Walled Struct., vol. 47, no. 6–7, pp. 692–700, 2009. DOI: 10.1016/j.tws.2008.11.009.

[55] S.A. Ponnusami, M. Gupta, and D. Harursampath, Asymptotic modeling of nonlinear bending and buckling behavior of carbon nanotubes, AIAA J., vol. 57, no. 10, pp. 4132–4140, 2019. DOI: 10.2514/1.J057564.

[56] D. Harursampath, and D.H. Hodges, Asymptotic analysis of the non-linear behavior of long anisotropic tubes, Int. J. Non-Linear Mech., vol. 34, no. 6, pp. 1003–1018, 1999. DOI: 10.1016/S0020-7462(98)00070-5.

[57] G. Brazier, On the flexure of 'thin' cylindrical shells and other thin sections, Proc. R Soc. A, vol. 116, pp. 104–114, 1927.

[58] W.H. Duan, Q. Wang, Q. Wang, and K.M. Liew, Modeling the instability of carbon nanotubes: from continuum mechanics to molecular dynamics, J. Nanotechnol. Eng. Med., vol. 1, no. 1, pp. 011001, 2010.

[59] V.M. Harik, Mechanics of carbon nanotubes: applicability of the continuum-beam models, Comput. Mater. Sci., vol. 24, no. 3, pp. 328–342, 2002. DOI: 10.1016/S0927-0256(01)00255-5.

[60] D. Harursampath, Non-Classical Non-Linear Effects in Thin-Walled Composite Beams, PhD dissertation, Georgia Institute of Technology, Atlanta, GA, USA, 1998.

[61] D.H. Hodges, Mixed variational formulation based on exact intrinsic equations for dynamics of moving beams, Int. J. Solids Struct., vol. 26, no. 11, pp. 1253–1273, 1990. DOI: 10.1016/0020-7683(90)90060-9.

[62] C.E.S. Cesnik, and S.-J. Shin, On the modeling of active helicopter blades, Int. J. Solids Struct., vol. 38, no. 10–13, pp. 1765–1789, 2001. DOI: 10.1016/S0020-7683(00)00135-9.

[63] T. Cheng, Structural Dynamics Modeling of Helicopter Blades for Computational Aeroelasticity, M. Tech thesis, Massachusetts Institute of Technology, Cambridge, MA, USA, 2002.

[64] C. Li, and T.W. Chou, Modelling of elastic buckling of carbon nanotubes by molecular structural mechanics approach, Mech. Mater., vol. 36, no. 11, pp. 1047–1055, 2004. DOI: 10.1016/j.mechmat.2003.08.009.

[65] S.I. Yengejeh, S.A. Kazemi, and A. Ochsner, Influence of combined loading on the structural stability of carbon nanotubes, Mater. Chem. Phys., vol. 158, pp. 96–106, 2015. DOI: 10.1016/j.matchemphys.2015.03.042.

[66] F. Mehralian, Y.T. Beni, and M.K. Zeverdejani, Calibration of nonlocal strain gradient shell model for buckling analysis of nanotubes using molecular dynamics simulations, Physica B, vol. 521, pp. 102–111, 2017. DOI: 10.1016/j.physb.2017.06.058.

Appendix: Mesh convergence and load sensitivity studies

Mesh convergence and load sensitivity studies were conducted, and the results are reported in this section. Different mesh sizes starting from 10 elements to 20, 50, 100, 200, 500, 1000 and 2000 elements were used. For cases of the current model, the convergence was observed for a normalized mesh size of 0.5. Here, the base mesh size taken was 1000 elements to establish the normalized mesh size. The mesh convergence study is represented in Figure 19.
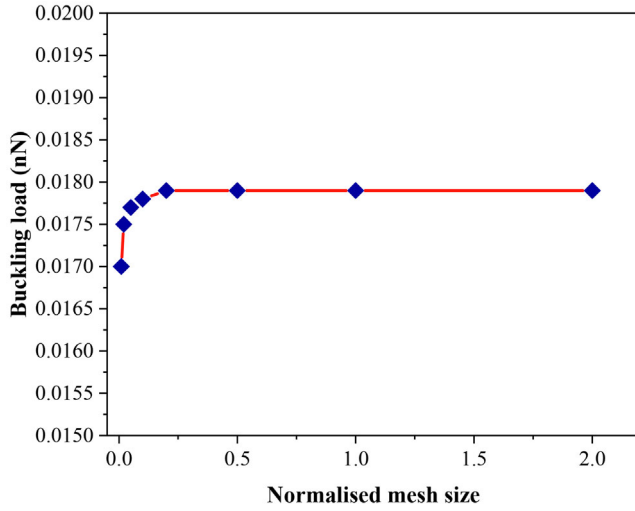
The CNT beam model is modeled as perfectly elastic, hence, to simulate the buckling behavior a very small transverse load is applied. It is a minimum load such that to ensure the buckling phenomena occurs and bending does not dominate the behavior of CNT. This loading was provided in the form of uniformly distributed load along one of the transverse directions. Therein it was found out that beyond the load of approximately $2*10^{-8}$ nN/nm, the changes in perturbation load leads to similar buckling load. Hence, this load was taken to simulate the buckling condition in CNT. However, the value of the perturbation load may vary with change in CNT length and thickness, the behavior remains same. This is as seen in Figure 20.
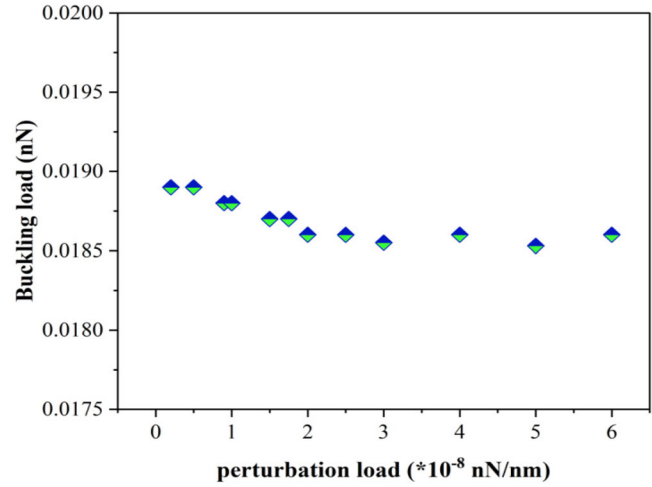

Figure 19. Mesh convergence study.

Figure 20. Load sensitivity study.